ISTITUTO NAZIONALE DI FISICA NUCLEARE

Sezione di Milano

INFN/TC-87/4

4 Maggio 1987

E. Fabrici and A. Salomone:

THE EXTRACTION SYSTEM FOR THE MILAN SUPERCONDUCTING CYCLOTRON

Servizio Documentazione
dei Laboratori Nazionali di Frascati

INFN - ISTITUTO NAZIONALE DI FISICA NUCLEARE
Sezione di Milano

INFN/TC-87/4
4 Maggio 1987

THE EXTRACTION SYSTEM FOR THE MILAN SUPERCONDUCTING CYCLOTRON

E. Fabrici and A. Salomone
Universita' degli Studi di Milano and INFN Sezione di Milano

ABSTRACT

This paper presents the extraction system chosen for the superconducting cyclotron under construction at the University of Milan and discusses the expected beam phase space characteristics.

1. - INTRODUCTION

This paper presents the extraction scheme chosen for the Milan superconducting cyclotron. The position and the number of the extraction elements are the result of an extensive analysis of the beam dynamics prior to extraction[1] and of the phase space behaviour through the extraction path for a set of representative ions. The extraction system consists of two electrostatic deflectors placed in two successive hills, followed by a set of magnetic channels of the passive type placed inside the vacuum chamber and throughout the cryostat traversal. A magnetic channel is also inserted in the yoke exit.

Peculiar to the Milan cyclotron design is the very wide dynamical range[2,3]. It is characterized by a variation of B_o, the nominal center field level for which the magnetic field can be isochronized, from $B_o \sim 48$ kgauss, corresponding to a $K_b = 800$ MeV, down to $B_o = 22$ kgauss. This poses some requirements on the design of the extraction hardware like:

-1) The first extracting elements, i.e. the electrostatic deflectors, must be radially movable over a range of about 3 cm. In fact, due to the limits on the electric fields obtainable on the deflectors, the high energy beams can be extracted only at a radius larger than R ~ 87 cm, while the low energy ones must be extracted at much more internal radii in order to avoid the $\nu_r + 2\nu_z = 3$ resonance[1].

-2) The electrostatic deflectors must be adjustable in shape due to the large differences in the scalloping of the extracted trajectories at the various field levels.

-3) Almost all the magnetic channels, which are passive and thus provide a field gradient independent from the main field level, must be removable from the extraction path. In this way it will be possible to scale the average focusing gradient provided by the extraction system with the main field level.

With respect to the earlier solution presented at the Caen Conference[4] the main difference is the radial position of the 1st electrostatic deflector, which has moved inward of about 9 mm. This is the result of more beam dynamic studies carried out with the use of magnetic field maps corresponding to the final cyclotron geometry [3]. Moreover the extraction trajectories are followed up to R = 216.6 cm, that is well outside the yoke.

The main characteristics of the extraction system are presented in the following together with an analysis of the phase space behaviour and the energy dispersion of the extracted beams.

2. - MAIN CHARACTERISTICS OF THE EXTRACTION SYSTEM

The extraction elements together with all the necessary penetrations are shown in Fig. 1, which presents a median plane view of the cyclotron up to R = 133.5 cm, i.e. the outer cryostat radius. The figure shows also the polar coordinate system used in all calculations (the clockwise increasing azimuth has been chosen in order to follow the particles motion). The two electrostatic deflectors E1, 52 degrees long from $\Theta = 104°$ to $\Theta = 156°$, and E2, 40 degrees long from $\Theta = 222°$ to $\Theta = 262°$, are placed in two successive

hills, the extracted beams being inside the dee in between. They are immediately followed by two magnetic channels: M1, 10 degrees long from $\Theta = 265°$ to $\Theta = 275°$, and M2, 6 degrees long from $\Theta = 279°$ to $\Theta = 285°$. A set of 5 magnetic channels, labelled M3 to M7 on Fig. 1, is placed along the extraction path in the fringing field of the following hill and through the cryostat traversal. All these channels are 6 degrees long and about equally spaced by 4 degrees. The large azimuthal clearance between M4 and M5 allows to insert a beam probe in a center hill position. Another magnetic channel, M8, is placed in the yoke traversal and so it is not shown in Fig. 1. The elements labeled as C1a, C1b and C2 are iron bars which compensate for the 1st harmonic field perturbation due to the magnetic channels from M1 to M7.

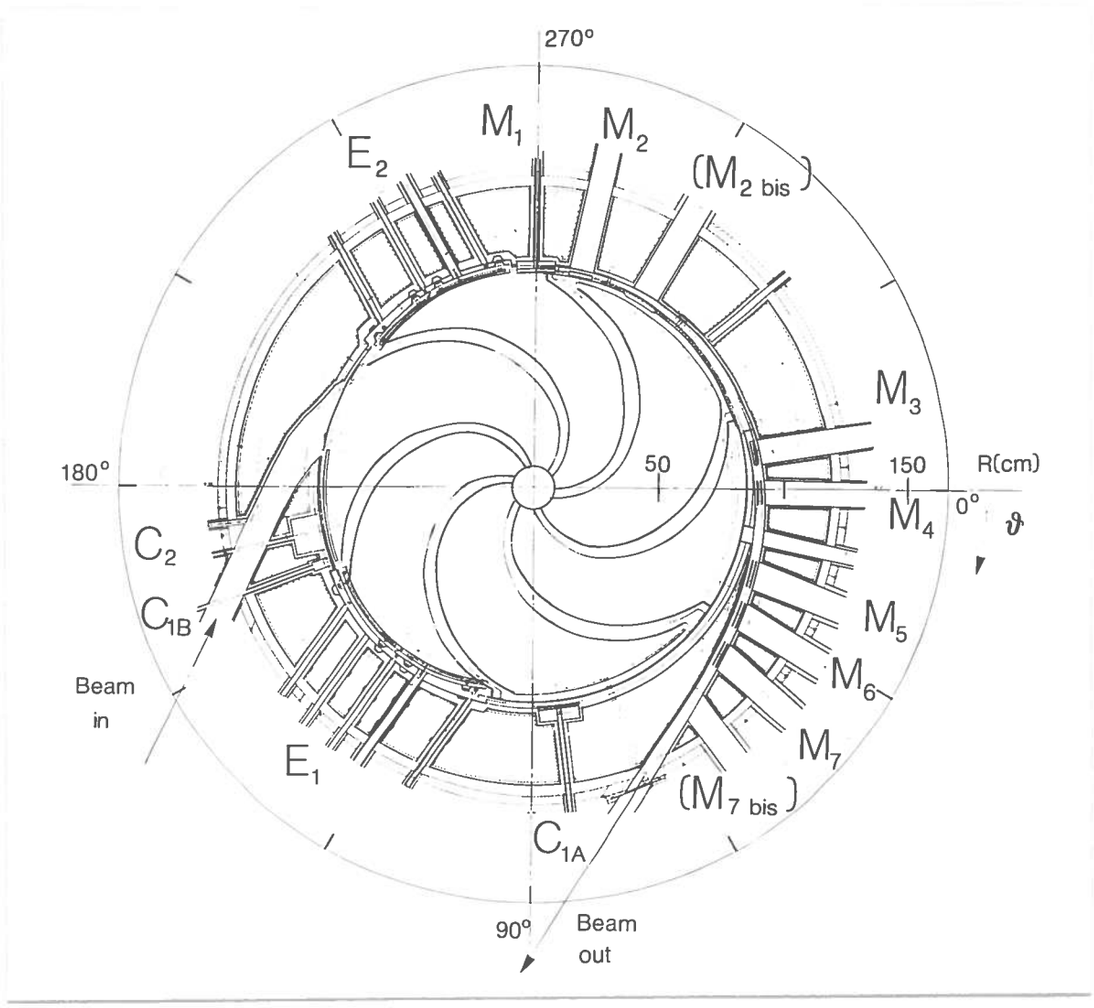

Fig. 1 - Median plane view of the cyclotron showing the extraction system.

Since the median plane penetrations through the cryostat have been drilled in from the beginning without waiting for the magnetic field measurements, the position of the extracting elements has been carefully investigated and, for the more critical points,

alternative solutions are provided. So two extra holes for the insertion of magnetic channels have been designed. One, labelled $M2_{bis}$ on Fig. 1 is from $\Theta = 296°$ to $\Theta = 304°$, while the other one, $M7_{bis}$, is from $\Theta = 50°$ to $\Theta = 56°$. Their possible use will be explained in the following paragraph on the orbits trajectories and the beams phase space behaviour.

The electrostatic deflectors, the channel M1 and the compensating bars will be mounted from the inside of the machine. Parallel penetrations have been chosen for the H.V. feedthroughs and the mechanical actuators of the electrostatic deflectors in order to easy their insertion. The magnetic channels, M2 to M7, will be mounted instead from the outside of the machine in order to allow their complete removal from the extraction path. The median plane penetrations through the yoke are schematically shown in Fig. 2 together with the three holes, labelled as coil support, necessary for the titanium rods used as radial suspension of the coils[5]. In the same figure the azimuth of the axis of each radial hole is also indicated.

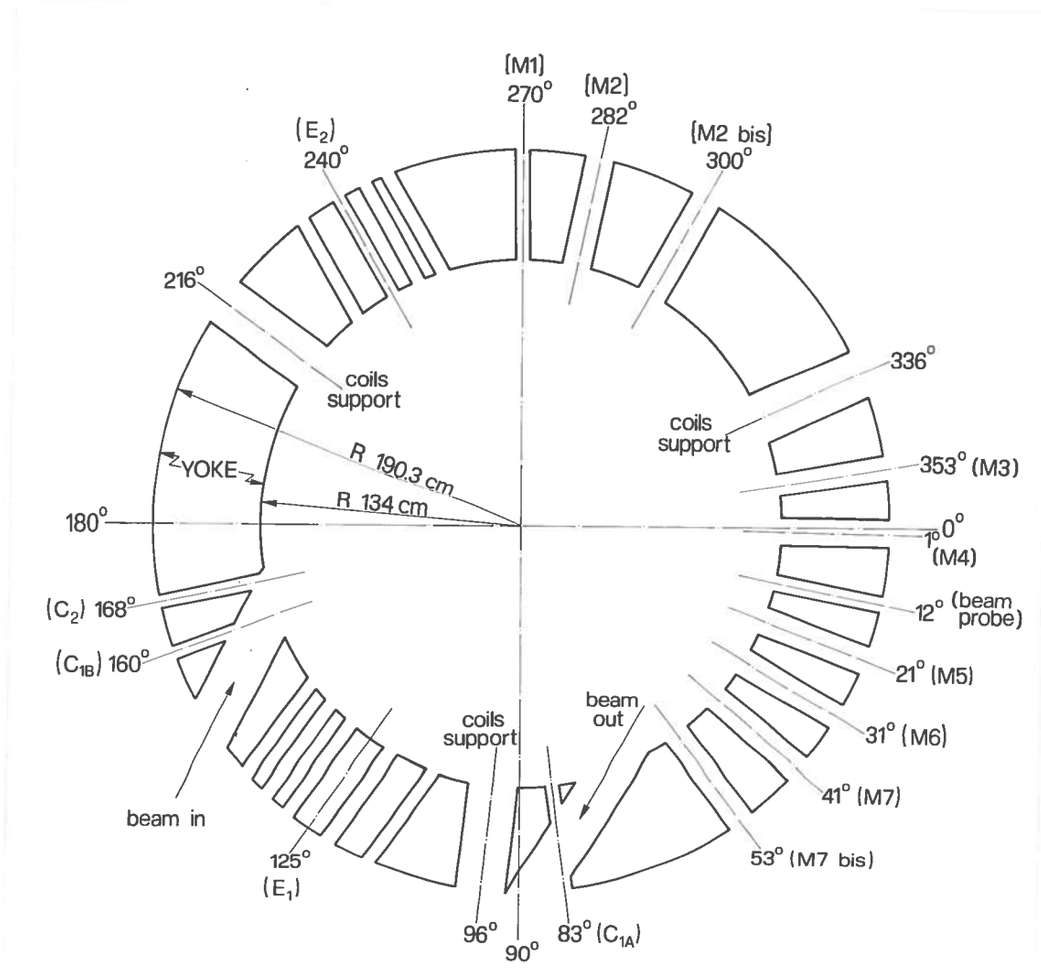

Fig. 2 - Median plane cross section of the yoke showing all the penetrations needed by the extraction system

Table I gives all the relevant parameters of the various extraction elements, i.e.:

- the initial and the final azimuths
- the average central ray position at the same azimuths
- the excursion around these average values, $\pm\Delta R$
- the maximum electric field needed on the electrostatic deflectors, Emax
- the field bias, ΔB, and the radially focusing gradient, $\partial B/\partial x$, provided by the magnetic channels as calculated in the approximation of uniform saturation of the iron bars.

Table I. - Extraction parameters

	Θ (deg)	R (cm)	$\pm\Delta R$ (cm)	Emax (kV/cm)	ΔB (kG)	$\partial B/\partial x$ (kG/cm)
E1	104.00 156.00	85.76 87.55	1.32 0.79	140.	-	-
E2	222.00 262.00	88.28 91.12	1.00 0.31	140.	-	-
M1	265.00 275.00	91.15 91.13	0.31 0.41	-	-2.0	3.86
M2	279.00 285.00	91.12 91.16	0.46 0.56	-	-1.8	3.12
M3	348.00 354.00	94.76 95.43	0.63 0.60	-	-1.2	3.63
M4	358.00 4.00	95.91 96.71	0.58 0.55	-	-1.2	3.63
M5	18.00 24.00	99.08 100.42	0.44 0.39	-	-1.2	3.63
M6	28.00 34.00	101.48 103.37	0.35 0.27	-	-1.2	3.63
M7	38.00 44.00	104.88 107.53	0.20 0.35	-	-1.2	3.63
M8	76.00 86.00	146.28 180.65	2.65 2.60	-	-2.0	0.75
C1a	78.00 88.00	94.65 94.65	1.75 1.75	-	-	-
C1b	158.85 161.00	94.65 94.75	1.75 1.75	-	-	-
C2	164.00 172.00	99.85 99.85	2.15 2.15	-	-	-

Fig. 3 shows in a Cartesian (R,Θ) plot the extraction trajectories up to the position of the channel M4 for the ions with charge to mass ratios Z/A = 0.5 and Z/A = 0.1 at the maximum and minimum energies. As mentioned above and apparent from Fig. 3 the ions extracted at the maximum and minimum field exhibit so different orbit scalloping inside the electrostatic deflectors as to require them to be adjustable in shape. In fact

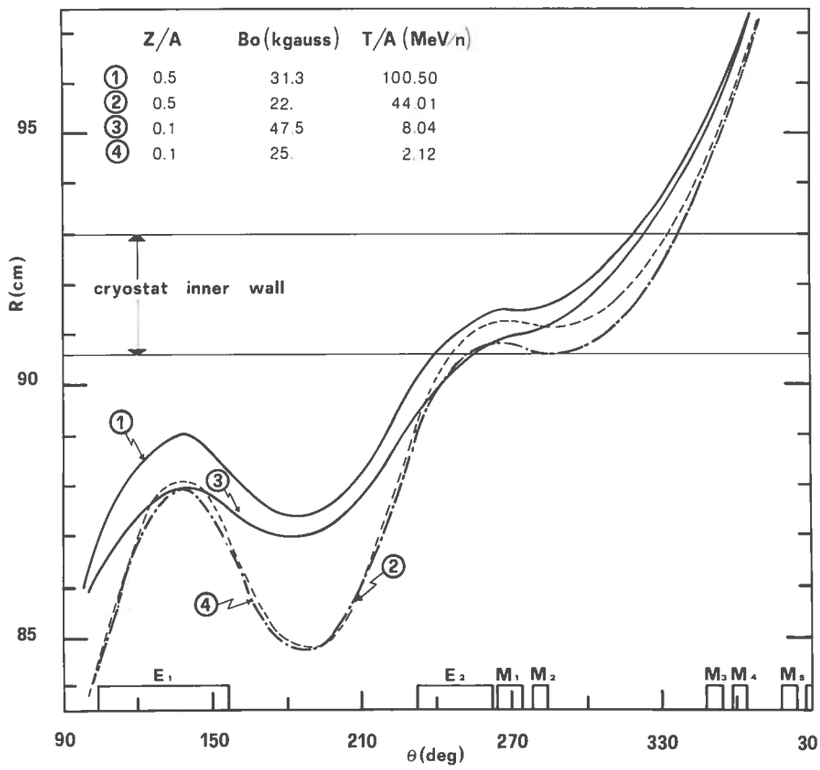

Fig. 3 - Extraction trajectories of four of the investigated ions on a cartesian (R,Θ) plot.

we have verified that with the Milan cyclotron geometry radially movable "rigid" deflectors, as adopted at M.S.U.[6], can be used only for center field levels ranging from the maximum, B_o ~ 48 kgauss, down to B_o ~ 31 kgauss and not down to the lower limit of B_o = 22 kgauss. Therefore the electrostatic deflectors are splitted in at least two parts connected by a swivel joint. The calculations[7] indicate that with one swivel joint approximately in the middle of E1, which has a linear length around 80 cm, we can fit the extraction trajectories throughout the operating range of the cyclotron within ±1.2 mm. This figure can be further reduced to ±0.6 mm by splitting the deflector in three parts connected by two joints. Only one joint is necessary instead in the shorter deflector, E2, in order to fit all the trajectories within ±0.5 mm.

Fig. 4 shows a view of the first electrostatic deflector together with the actuators for the radial movements and the high voltage feedthrough. The three actuators are positioned at the deflector entrance, at the swivel point and at the exit. The hole

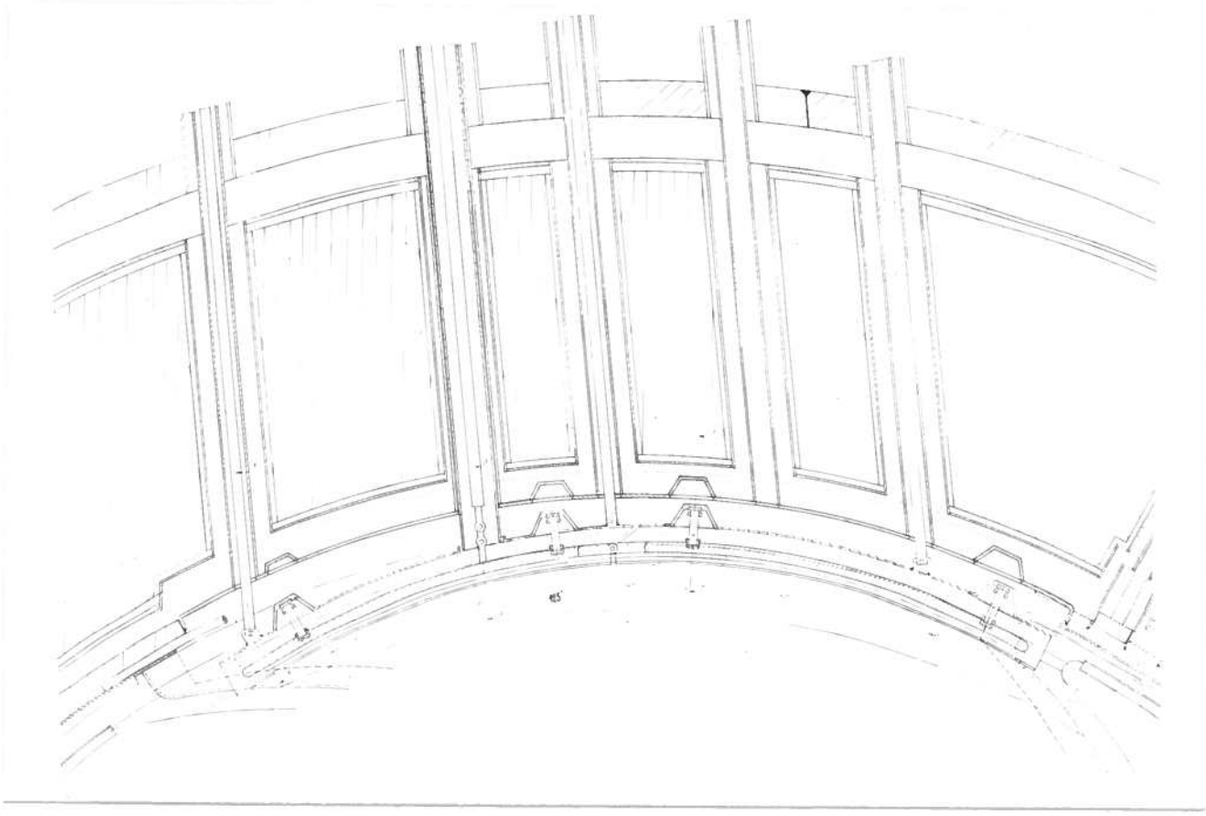

Fig. 4 - View of the 1st electrostatic deflector.

between the swivel point and the last actuator, which is shown empty in Fig. 4, will eventually allow the use of the second joint. In this case the high voltage feedthrough will be moved to the central hole, thus placing the two joints approximately at one third and two thirds of the deflector length. A box-like solution has been chosen for the electrostatic deflectors with a vertical sparking distance of 54 mm and an electrode septum gap of 8 mm. Since the maximum electric field required is 140 KV/cm the deflectors must hold a voltage of 112 KV. The results obtained on a prototype deflector are given in Ref. 8. Fig. 5 shows a vertical cross section of the first electrostatic deflector at Θ = 106° in correspondence of the 1^{st} actuator. The dot represents the beam, while the numbers on the figure give the deflector radial position for extraction of a low center field ion, i.e. Z/A = 0.1 and B_o = 25 kgauss, corresponding to the more inward deflector position. The radial movement allowed at this azimuth is 34.5 mm as shown by the dashed line marking on the figure the more outward deflector position. Fig. 6 shows a vertical cross section

of the 1st electrostatic deflector at $\Theta = 134°$ in correspondence of an insulator. Four of these are needed to hold the high voltage electrode.

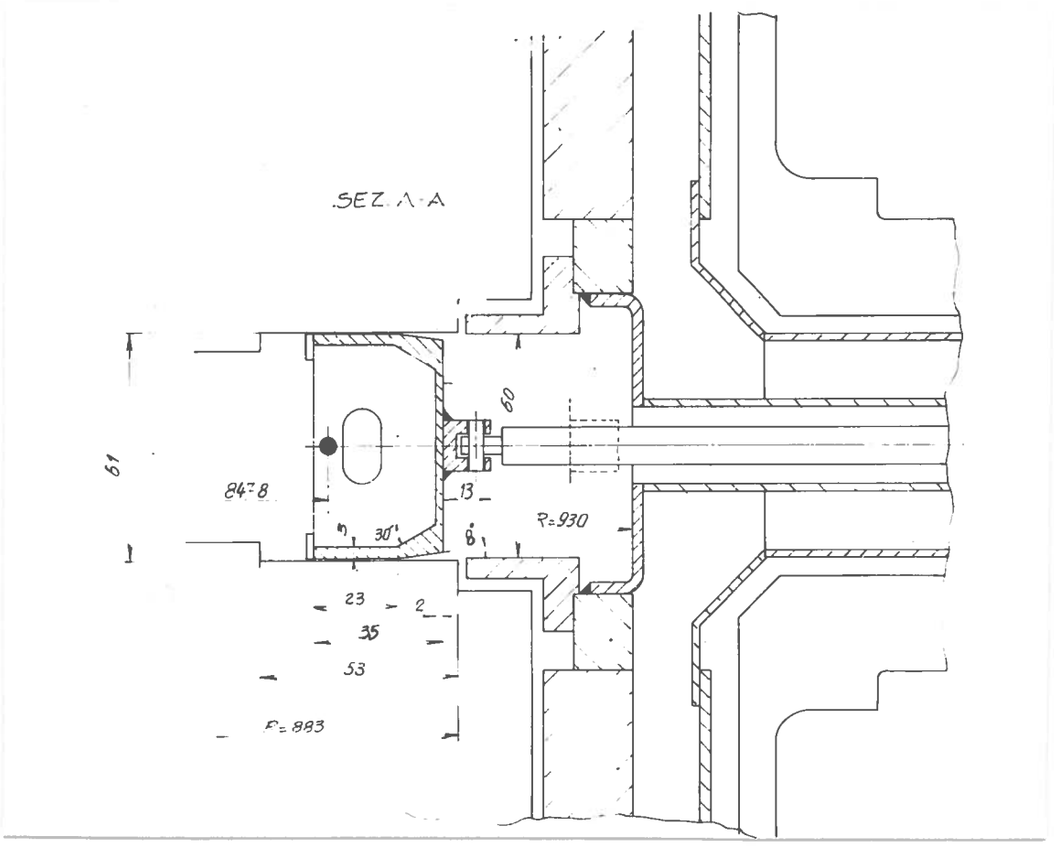

Fig. 5 - Vertical cross section of the 1st electrostatic deflector at the location of one of the mechanical actuators. The dot marks the beam position. The dashed line indicates the outermost position of the deflector.

All the magnetic channels M1 through M7 are made with iron bars since in this way large radially focusing gradients can be obtained in channels of reduced vertical dimensions. In fact, although the cryostat midplane ring is 12 cm high, the radial holes drilled through it can have only a limited height because the ring must withstand the compressive forces exerted by the coils (at the maximum coils excitation the pressure on the ring is estimated to be ~ 150 kg/cm^2 (9)). Therefore the maximum vertical height of the channels has been limited to 30 mm. The schematical cross section of the channels is presented in Fig. 7. Since the requirements on the field bias and on the radial focusing of the channels are different along the extraction path three different geometries exist: one for M1, another for M2 and a third one for the channels from M3 to M7. Fig. 8 gives a more detailed vertical cross section of M6 at $\Theta = 32°$, showing also the 35 mm pipe through which the channel is inserted.

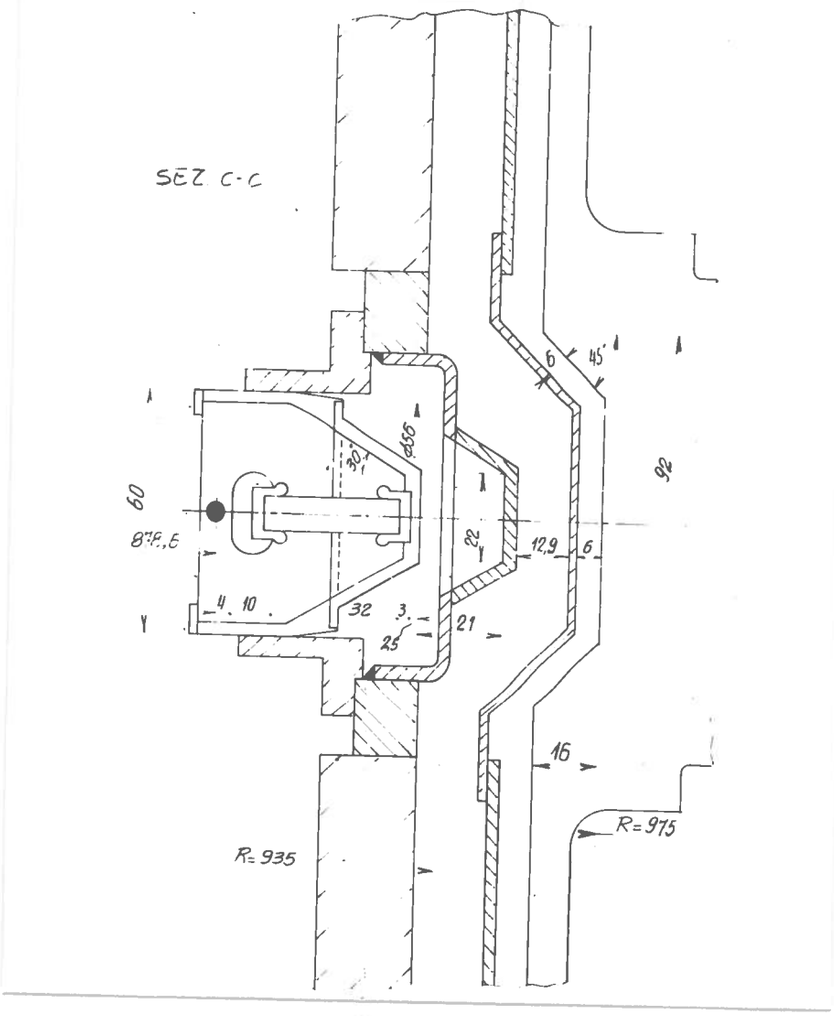

Fig. 6 - Vertical cross section of the 1st electrostatic deflector at the location of one of the insulators. The dot marks the beam position.

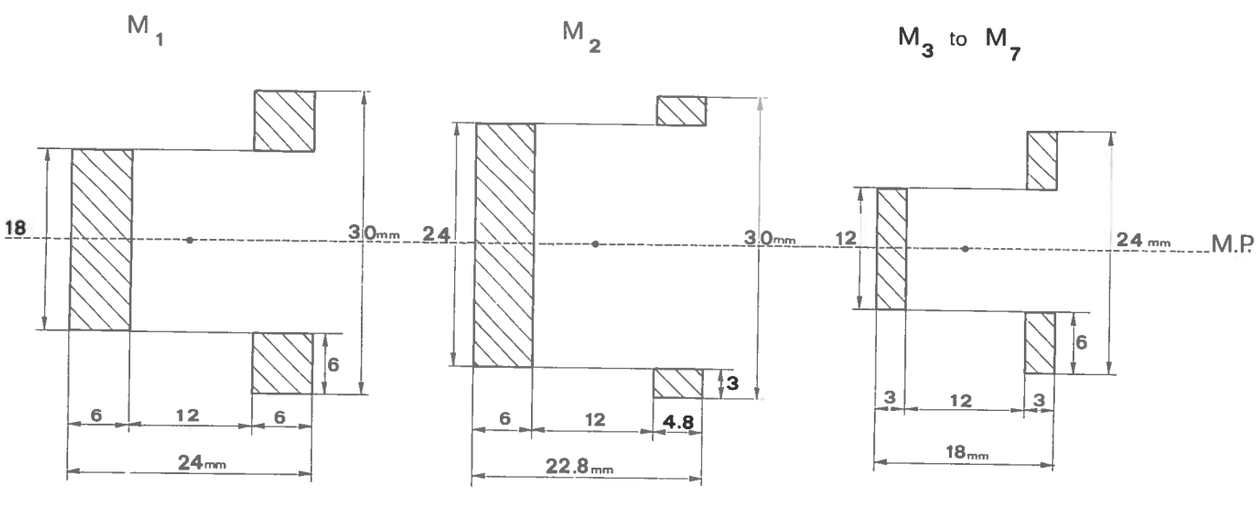

Fig. 7 - Schematic cross section of the magnetic channels M1, M2 and M3 to M7. The dots in the middle mark the beam positions.

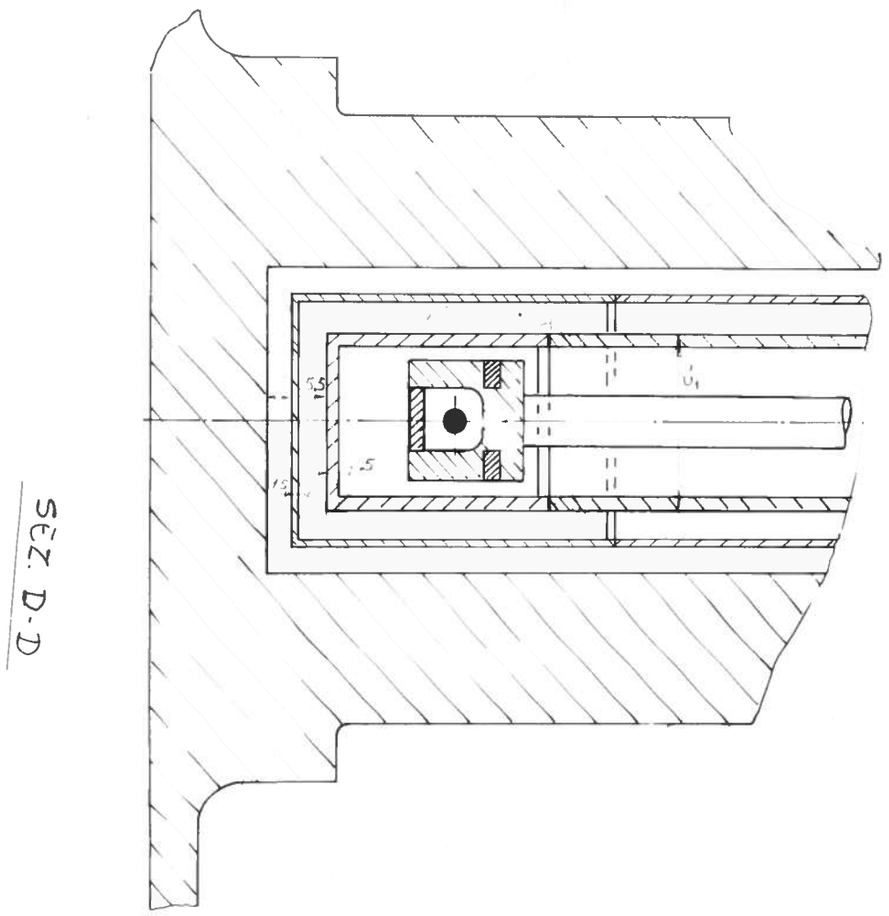

Fig. 8 - Vertical cross section of the channel M6. The dot marks the beam position.

For the magnetic channel M8 needed in the yoke traversal no firm choice has been made so far between a passive or an active one. The present calculations envisage a passive channel as schematized in Fig. 9. The channel useful width is large enough, 8.3 cm, in order to accomodate all beams without moving the channel itself.

The compensating bars are straight iron bars whose cross sections are shown in Fig. 10. Fig. 11 presents instead a more detailed cross section of C2 at $\Theta = 168°$ showing also the dee and the liner positions. The bar is drawn with a solid line at its innermost radial position while the dotted line indicates its outermost position. The bars C1a and C1b, which have the same cross section, together compensate for the 1^{st} harmonic field perturbation produced by the channels M1 and M2. Two bars are required because the radial coils support centered at $\Theta = 96°$ (see Fig. 2) prevents the insertion of a single bar exactly 180° apart from M1 and M2. The bar C2 compensates for all the remaining channels from M3 to M7[1]. No investigation of the field perturbation due to M8 has been done since the latter channel is far away from the $\nu_r = 1$ resonance and has thus a negligible effect on the internal beams dynamics.

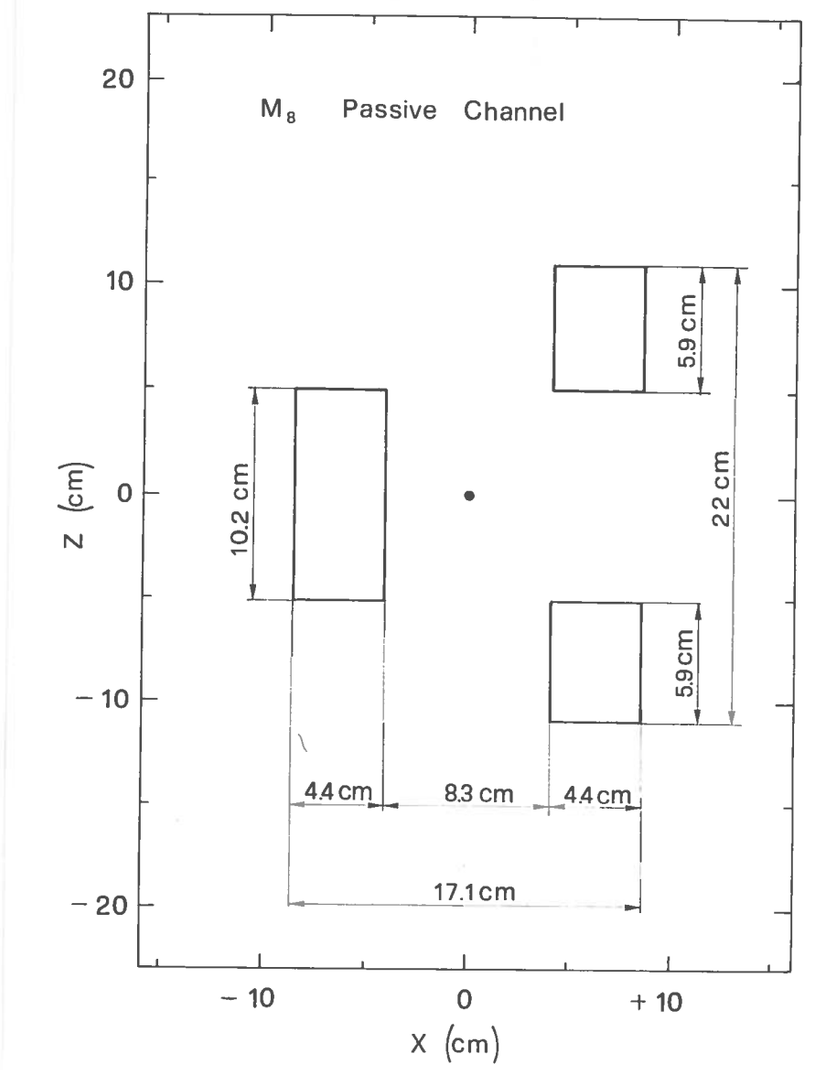

Fig. 9 - Schematic cross section of the magnetic channel M8.

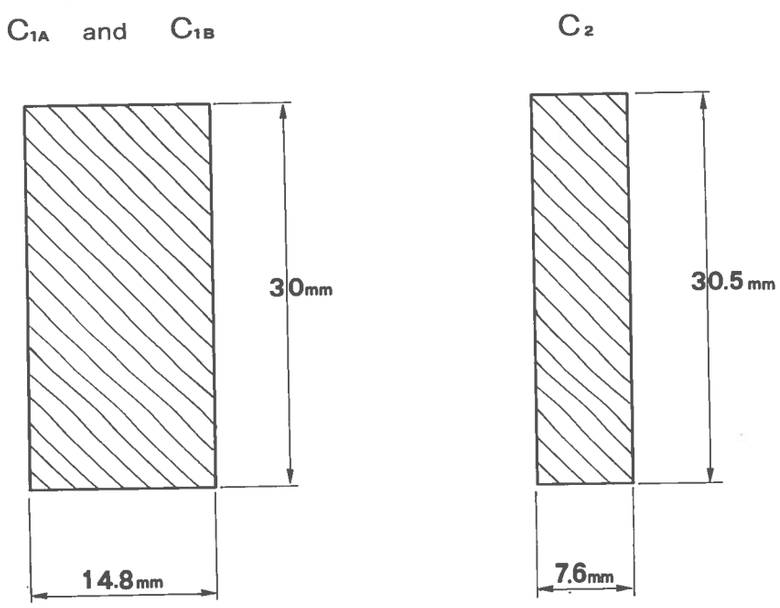

Fig. 10 - Schematic vertical cross section of the compensating bars. On the left side the cross section of the bars C1a and C1b, on the right side the cross section of the bar C2.

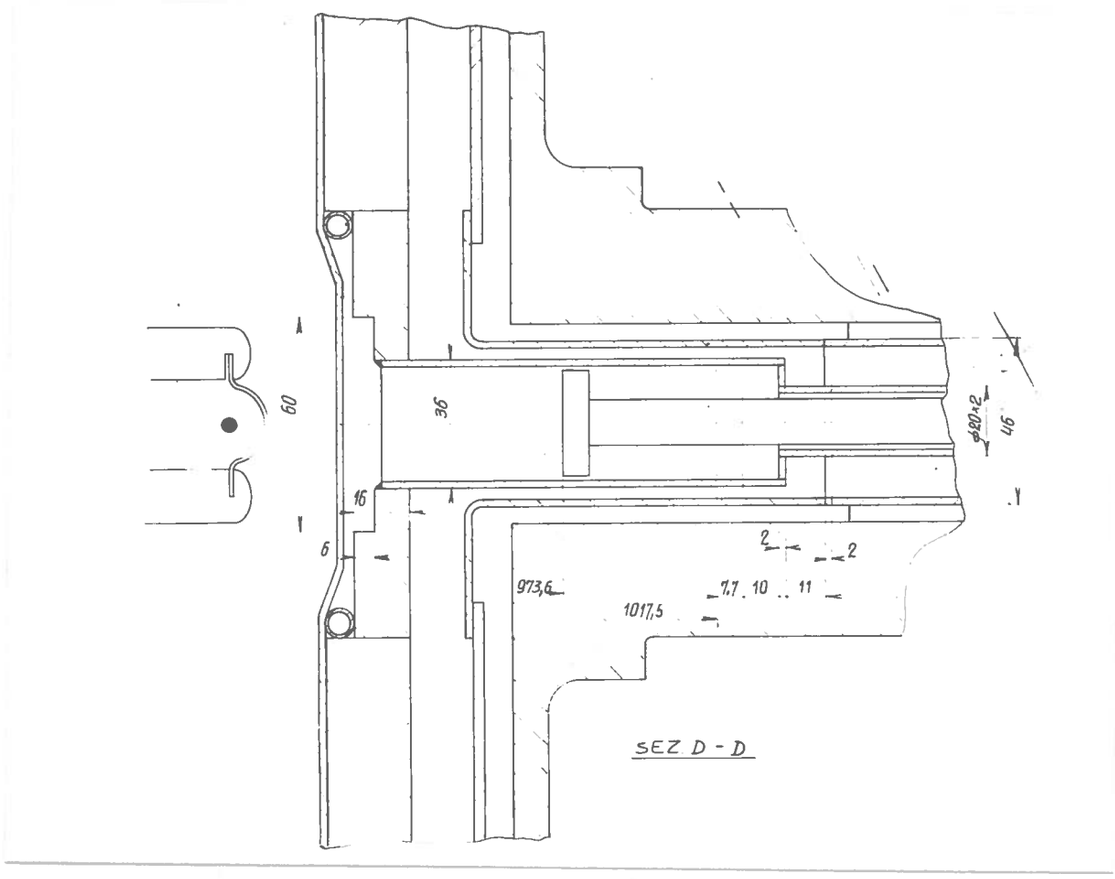

Fig. 11 - Vertical cross section of C2 at $\Theta = 168°$, showing also the dee and the liner.

3. - PERFORMANCES

The extraction scheme has been designed analysing the central rays trajectories and the phase space behaviour of twelve beams representative of the entire cyclotron operating range. The selected ions are shown by dots on the cyclotron operating diagram in the $(Z/A, B_o)$ plane of Fig. 12 and they are listed in order of decreasing charge to mass ratio and center field value in Table II. Their energy, T/A in MeV/n, is also given. Eight ions have been chosen along the contours of the operating diagram in order to investigate the more critical situations. Labelling each beam with just its charge to mass ratio and the B_o value in kgauss with the notation $(Z/A/B_o)$ they are the ions 0.1/47.5 and 0.25/45.5 along the bending limit (K_b = 800 MeV), the ions 0.3/41.4 and 0.5/31.3 along the focusing limit (K_{foc} = 200 MeV), the ions 0.5/22, 0.4/22, 0.3/22, 0.1/25 at low fields where the effects of the $\nu_r + 2\nu_z = 3$ resonance are more important. The other ions in the middle of the diagram (0.25/40, 0.25/38, 0.25/30 and 0.5/26.5) were studied mainly to check the feasibility of the extraction system at all field levels and especially the choice of having the magnetic channel M2 immediately after M1.

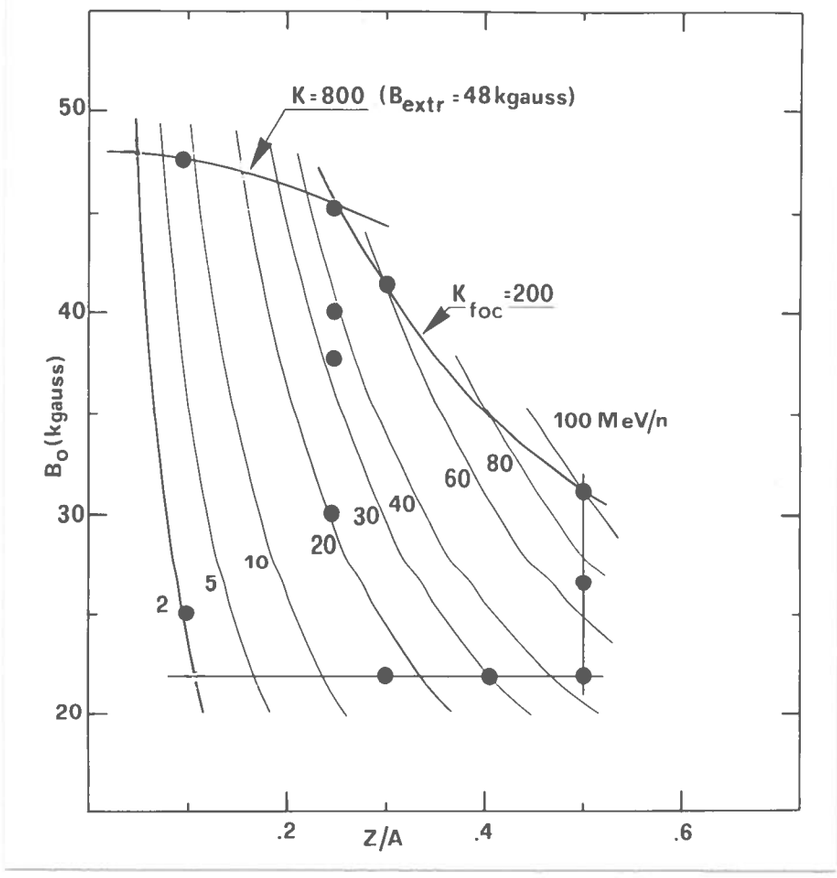

Fig. 12 - Cyclotron operating diagram in the ($Z/A, B_o$) plane. The dots indicate the ions chosen for this study. Lines of constant T/A are also shown.

Table II. -
Representative ions used for this study

Z/A	B_o (kgauss)	T/A (MeV/n)
0.5	31.3	100.50
	26.5	67.18
	22.0	44.01
0.4	22.0	27.59
0.3	41.4	59.63
	22.0	15.12
0.25	45.5	49.42
	40.0	37.15
	38.0	33.23
	30.0	20.19
0.1	47.5	8.04
	25.0	2.12

3.1. - Calculation methods

The extracted orbits have been tracked by performing Runge-Kutta integration generally with integration steps of 2 degrees. For the final calculations an integration step of 1 degree has been adopted in order to better define the profiles of the electrostatic deflectors and of the extraction channel throughout the cryostat. The starting conditions at Θ = 100°, azimuth close to the entrance of the 1st electrostatic deflector, were determined for each beam by the extensive analysis of the internal beam dynamics reported in Ref. 1.

These extraction calculations use three-fold, 120° symmetric field maps extending outside the yoke up to R = 231 cm. Inside the cryostat, i.e. up to R = 130 cm, the fields are as calculated as reported in Ref. 3. From these fields we have subtracted the average field produced by the magnetic channels and the compensating bars, which is plotted in Fig. 13 as a function of the radius from R = 76 cm to R = 92 cm. This field, which is opposite in sign with respect to the main field and not negligible in the region between 80 and 85 cm, is included in the field isochronizing process in order to optimize the final phase of the extracted beams[3,1]. However it cannot be included in the field maps used for the extraction calculations since the fringing field of the magnetic channels and of the iron bars is different from zero only at azimuths very close to the elements themselves. This can be seen in Fig. 14 where the field is plotted as a function of the azimuth from Θ = 100° to Θ = 200° at three radii relevant for the extraction, i.e. R = 86, 88, and 90 cm. It is apparent from the figure that the field produced by the bars C1b and C2 does not reach the inside of the 1st electrostatic deflector. Instead by using the field maps of Ref. 3 an average field bias of a few tens Gauss would have been present along the 1st electrostatic deflector, thus making extraction easier.

The extension of the field maps through the yoke traversal use the results of field calculations with the relaxation code POISCR[10]. In these calculations the median plane penetrations through the yoke are simulated by an air ring of equivalent volume extending from R = 155 cm to R = 165 cm and with an heigth from the midplane of 12.5 cm. The field values obtained inside this air ring, B_{yoke}, are parametrized in Fig. 15 as a function of $2.8J_{\alpha} + J_{\beta}$, where J_{α} and J_{β} are the average current densities in the two main coil sections[2]. Since the results look reasonable when compared with the fields measured

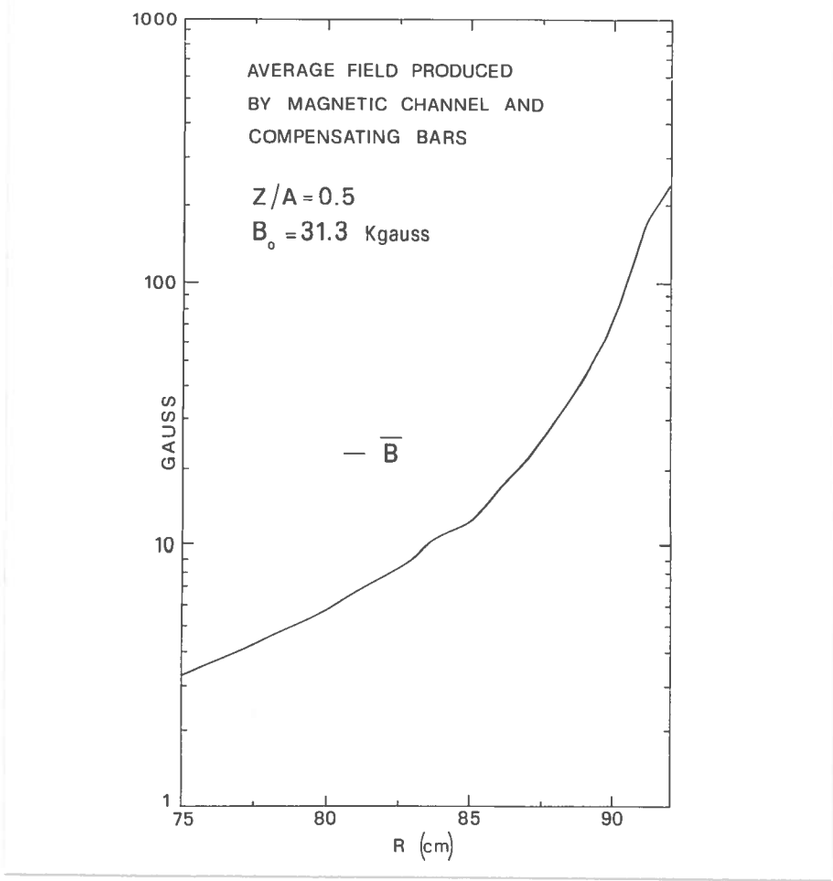

Fig. 13 - Average field produced inside the cyclotron by the magnetic channels and the compensating bars. The negative sign implies that this field is opposite to the main field.

inside the yoke extraction channel at M.S.U[10] and lacking other magnetic field measurements we have decided to use the B_{yoke} values given in Fig. 15 as field along the yoke traversal. Obviously, for each field level, we carried out a smooth matching with the average field calculated as reported in Ref. 3 up to R = 130 cm. As an example Fig. 16 shows the average field as a function of the radius from R = 110 cm to R = 230 cm for six of the investigated ions. The fringing field outside the machine ($R \geq 190$ cm) has been obtained by matching the B_{yoke} values with the fields given by the same POISCR calculations at R ~ 220-230 cm.

All the extraction elements are approximated by field biassis extending along the central rays trajectories from the initial to the final deflector azimuths. The electric field inside the deflectors is replaced by an equivalent magnetic field bias, B_{eq}, as given by $B_{eq} = E/v$, where E is the electric field and v the ions velocity. The field

produced by the magnetic channels is calculated by assuming uniform saturation of the iron bars[11]. These calculated fields are plotted as solids lines in Fig. 17 for the channels M1, M2, and M3 throu M7. In the figure the x coordinate is assumed to be perpendicular to the central ray trajectory, the x=0 position being the geometrical center of the channel and the central ray position. The dashed areas indicate the maximum expected radial dimension of the beams. The field gradients $\partial B/\partial x$ are plotted as dashed lines to show the linearity of the fields inside the channels. Although deviations from linearity are almost negligible, all phase space calculations presented in the following use the fields shown in Fig. 17 without approximating them with perfectly linear fields as was done in Ref. 6,4. No appreciable worsening of the radial phase space has been however observed if these calculations are compared with those of Ref. 4.

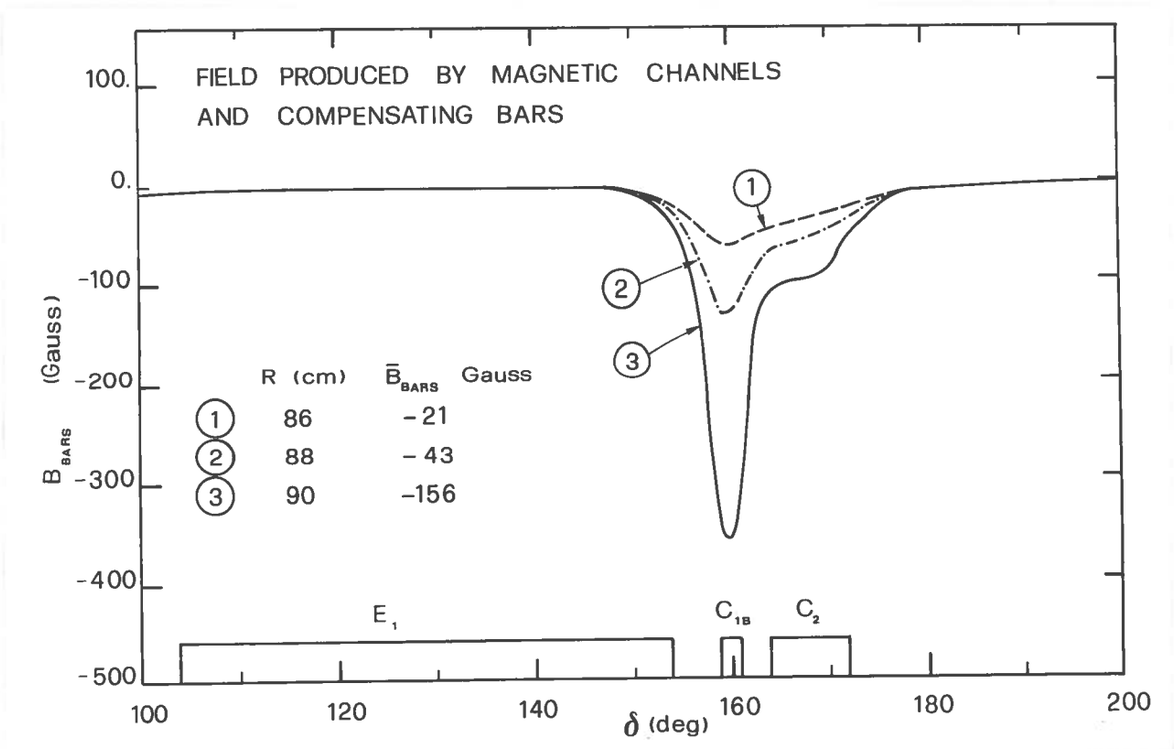

Fig. 14 - Field produced by the magnetic channels and the compensating bars plotted as a function of the azimuth from $\Theta = 100°$ to $\Theta = 200°$ at three radii relevant for the extraction. At the same radii are also indicated the values of the field when averaged over 360 degrees.

The field and the field gradient produced by the channel M8, which is in the yoke traversal, are shown in Fig. 18 for the channel geometry presented in Fig. 9. Obviously the assumption of complete saturation of the iron bars is not true at all field levels since the expected fields inside the yoke hole range from -6 kgauss to zero as presented

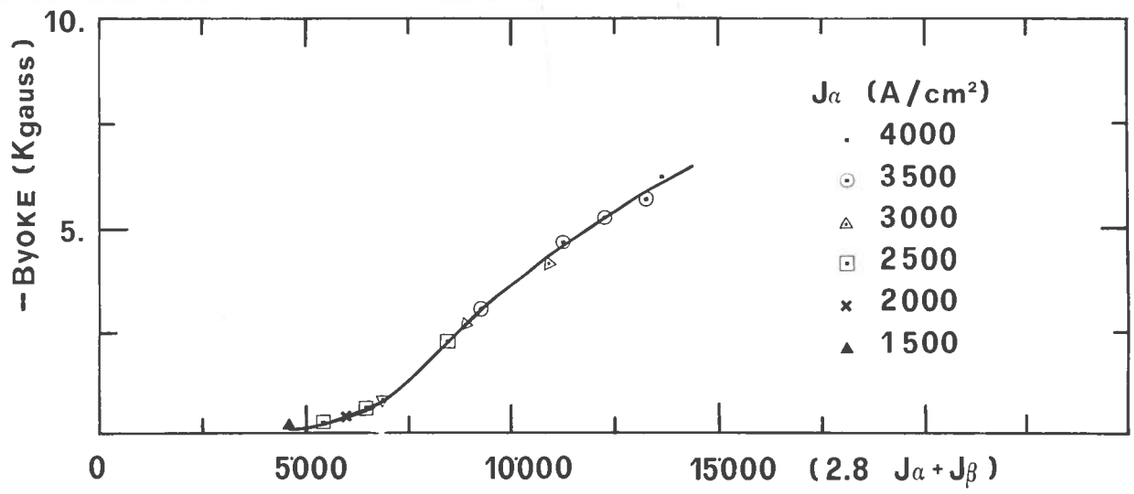

Fig. 15 - Field in the yoke hole provided for extraction as calculated with a magnetostatic model (see text for details). J_α and J_β are the current densities in the two main coils sections α and β, the α section being the closer to the median plane.

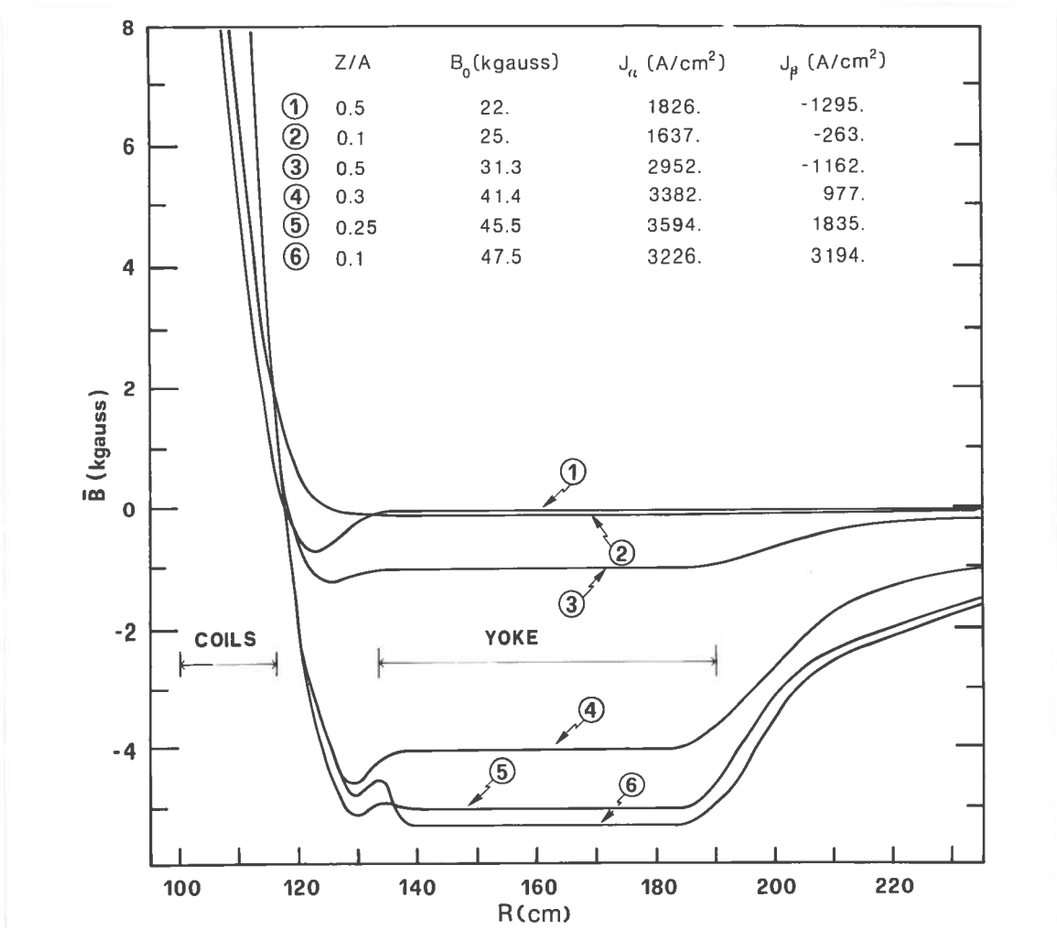

Fig. 16 - Calculated average field plotted as a function of the radius from R = 110 cm to R = 230 cm for six of the investigated ions.

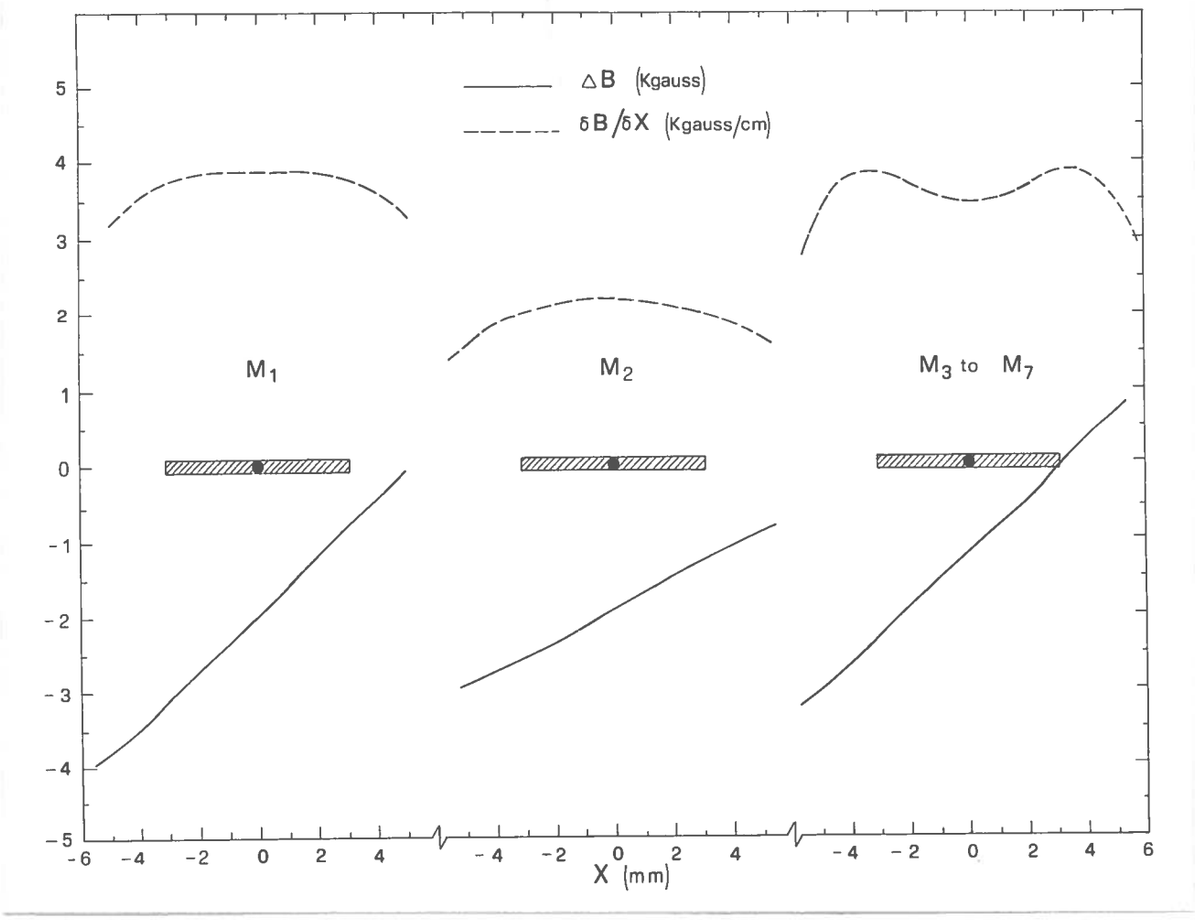

Fig. 17 - Fields (solid lines) and transverse field gradients (dashed lines) inside the passive magnetic channels M1 to M7 (see Fig. 8 for the channels geometry) as calculated assuming uniform saturation of the iron bars . The x = 0 position marks the central ray position, while the dashed area indicates the maximum expected radial width of the beams.

in Figs. 15 and 16. So the assumed field gradient is scaled with the external B_{yoke} field following the data measured at M.S.U.[10], i.e. we have chosen a field gradient corresponding to that of full saturation when B_{yoke} is at least -4 - 5 kgauss, 0.37 times the full saturation value when B_{yoke} is around -1 kgauss and no field gradient when B_{yoke} is less than 1 kgauss. As a reference Table III lists for the ions along the borders of the cyclotron operating diagram the B_{yoke} values and the field gradients assumed inside M8. In the absence of measured data for this channel we further assume that the radial focusing gradient is constant over the entire region occupied by the beams. Moreover no field bias exists at the central ray positions.

In all calculations the deflectors fields are approximated by hard edge fields. As an example Fig. 19 shows the field bias and the transverse field gradient plotted along the axis of M1 (the channel axis being coincident with the central ray trajectory) from the channel center (y=0) up to 4 cm outside the channel. The dashed lines represent the

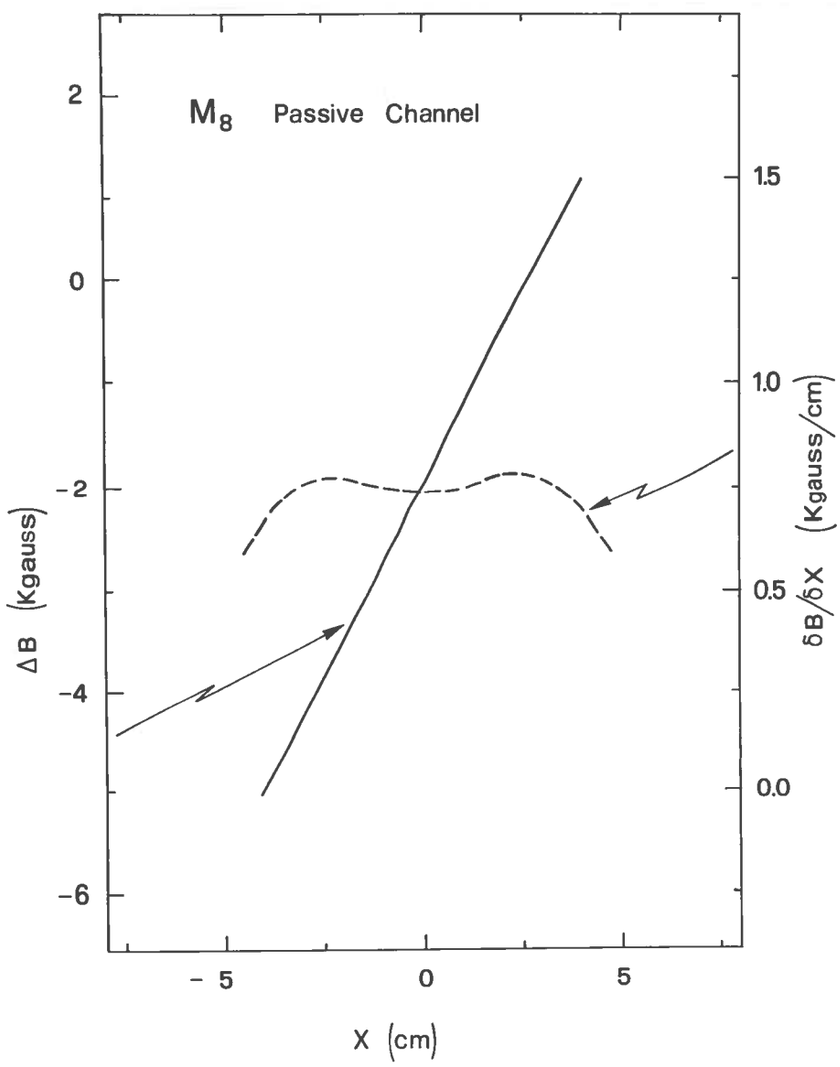

Fig. 18 - Field (solid line) and transverse field gradient (dashed line) inside the magnetic channel M8 (see Fig. 9 for the channel geometry) as calculated assuming uniform saturation of the iron bars.

Table III. -
Extimated field in the yoke hole
and field gradient in M8

Z/A	B_o (kgauss)	B_{yoke} (kgauss)	$\partial B/\partial x$ (kG/cm)
0.5	31.3	-1.0	0.27
	22.0	-0.1	0.
0.4	22.0	-0.1	0.
0.3	41.4	-4.0	0.75
	22.0	-0.1	0.
0.25	45.5	-5.0	0.75
0.1	47.5	-5.3	0.75
	22.0	-0.1	0.

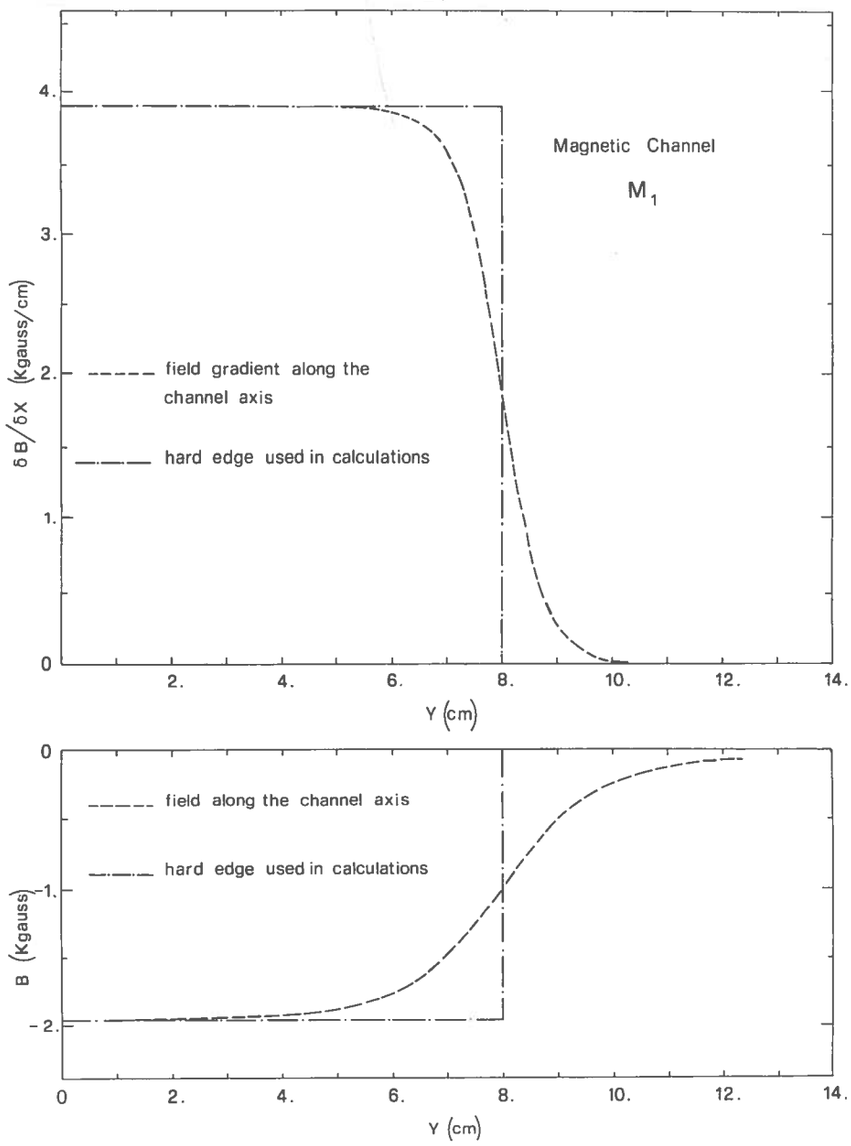

Fig. 19 - Field (lower plot) and transverse field gradient (upper plot) along the axis of the magnetic channel M1 as calculated assuming uniform saturation of the iron bars and their hard edge approximation used in the extraction calculations.

field and the field gradients calculated by assuming uniform saturation of the iron bars, while the point-line curves are their hard edge approximation. The effective length of the channel is longer than the physical one since the fringing field outside the channel compensates almost exactly for the smooth decrease of the field inside the channel. Therefore no overestimate of the average field bias is made.

3.2. - The extraction trajectories

As a reference Table IV lists the starting conditions at $\Theta = 100°$ for all the central rays. They are given in the usual terms: the radius R and the radial component of

Table IV. - Central ray data at $\Theta = 100°$

Z/A	B_o (kgauss)	R (cm)	p_r (cm)	T/A (MeV/n)	α (deg)
0.5	31.3	86.531	6.469	100.417	46.56
	26.5	85.005	7.966	67.097	-0.29
	22.0	83.749	9.805	43.923	4.50
0.4	22.0	84.171	9.908	27.483	2.42
0.3	41.4	86.429	4.795	59.574	28.88
	22.0	83.796	9.674	15.038	-1.69
0.25	45.5	86.782	4.293	49.370	34.16
	40.0	85.848	5.193	37.108	-1.24
	38.0	85.748	5.526	33.262	6.27
	30.0	85.753	6.944	20.218	14.18
0.1	47.5	85.922	4.392	8.013	13.64
	25.0	83.797	8.762	2.118	-3.48

the momentum p_r in cm, the energy T/A in MeV/n and final phase with respect to the R.F. phase Φ in degrees. The energies listed here are slightly lower than the extracted energies given in Table II due to the three accelerating gap crossings between $\Theta = 100°$ and the exit from the vacuum chamber. The central rays starting conditions at the entrance of the 1^{st} electrostatic deflector are summarized in Fig. 20 showing for each of the investigated ions the radius at $\Theta = 104°$, R, and the angle, α, between the central ray direction and the tangent to a circle of radius equal to R (i.e the angle defined by $\sin(\alpha) = p_r/p$). As already anticipated in Table I the central ray radial positions span 3 cm, with the higher rigidity beams being grouped near the maximum extraction radius. The trajectories of these last ions show deviations from a circular trajectory which are around 3°, while the beams with B_o = 22 kgauss enter the deflector with an angle α close to 7°.

By properly adjusting the electric field of E1 and E2 all the beams are made to converge to a common point 25 cm outside the yoke, where the first element of the beam transport line can be placed. The envelope of all the extracted beams throughout the yoke up to their common exit point at $\Theta = 92°$ and R = 216.60 cm is shown in Fig. 21.

For all the beams along the borders of the cyclotron operating diagram Table V lists the central ray radial positions at the entrance, at the middle point and at the exit of the two electrostatic deflectors, at the middle of the magnetic channels M1 thru M7, at the entrance and at the exit of M8. The same table also gives the radial position

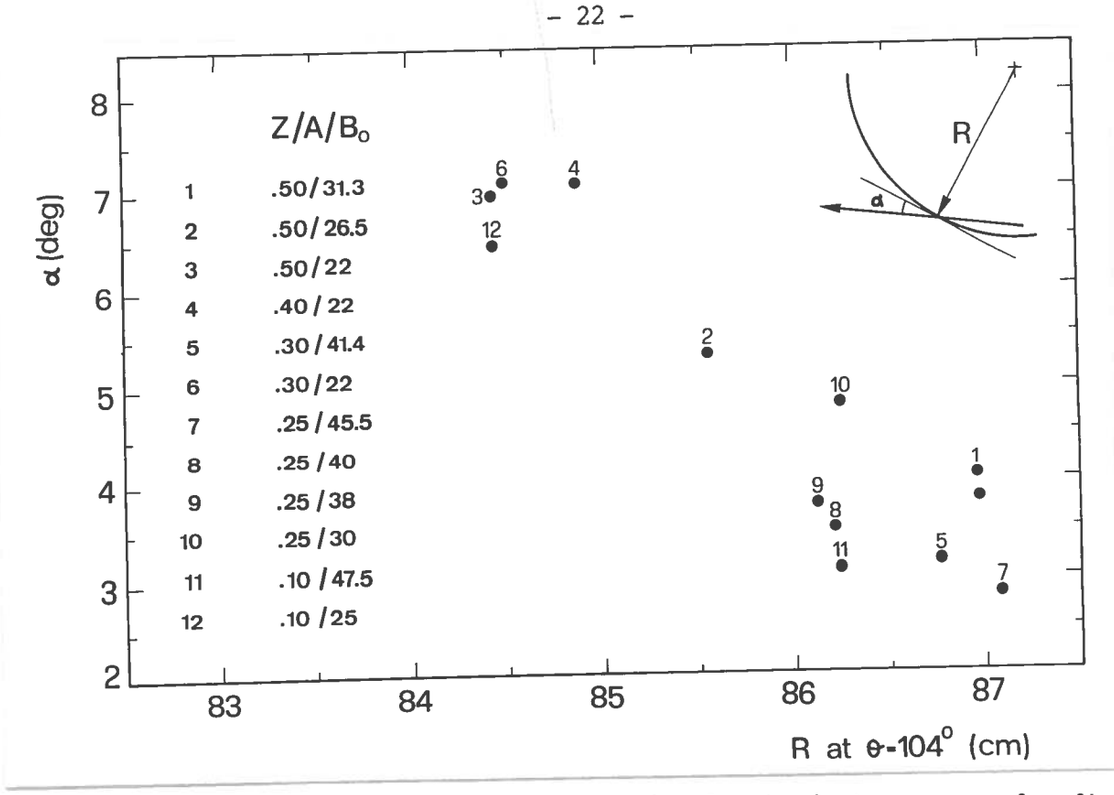

Fig. 20 - Angular divergency with respect to a circular trajectory, α and radial position at the entrance of the 1st electrostatic deflector for all the investigated ions.

Table V. - Central ray data for eight representative ions

	Θ (deg)	.5/31.3	.5/22	.4/22	.3/41.4	.3/22	.25/45.5	.1/47.5	.1/25
E1	104.	86.96	84.44	84.88	86.76	84.50	87.08	86.24	84.44
	130.	88.89	87.97	88.33	88.37	88.02	88.52	87.83	87.72
	156.	88.34	87.01	87.19	88.11	86.85	88.28	87.56	86.77
E2	222.	89.22	87.69	87.66	89.15	87.28	89.28	88.63	87.56
	242.	90.73	90.26	90.22	90.50	89.99	90.53	90.04	89.98
	262.	91.43	91.25	91.09	91.28	90.95	91.26	90.81	90.84
M1	270.	91.50	91.26	91.03	91.44	90.90	91.42	90.96	90.80
M2	282.	91.57	91.16	90.82	91.65	90.70	91.63	91.13	90.63
M3	351.	95.59	94.74	94.48	95.70	94.52	95.70	95.35	94.56
M4	1.	96.78	96.01	95.72	96.86	95.81	96.86	96.56	95.83
M5	21.	100.14	99.63	99.29	100.10	99.34	100.10	99.93	99.46
M6	31.	102.68	102.31	102.06	102.52	102.10	102.50	102.41	102.28
M7	41.	106.33	106.09	106.02	105.93	106.09	105.88	105.88	106.33
	68.	130.79	131.49	131.57	128.37	131.70	128.02	128.13	132.05
M8	76.	147.39	148.47	148.53	144.18	148.64	143.65	143.63	148.92
	86.	181.94	183.02	183.05	178.82	183.11	178.22	178.06	183.25
	88.	191.88	192.76	192.77	189.31	192.82	188.80	188.64	192.92
	92.	216.60	216.61	216.59	216.59	216.59	216.60	216.59	216.61

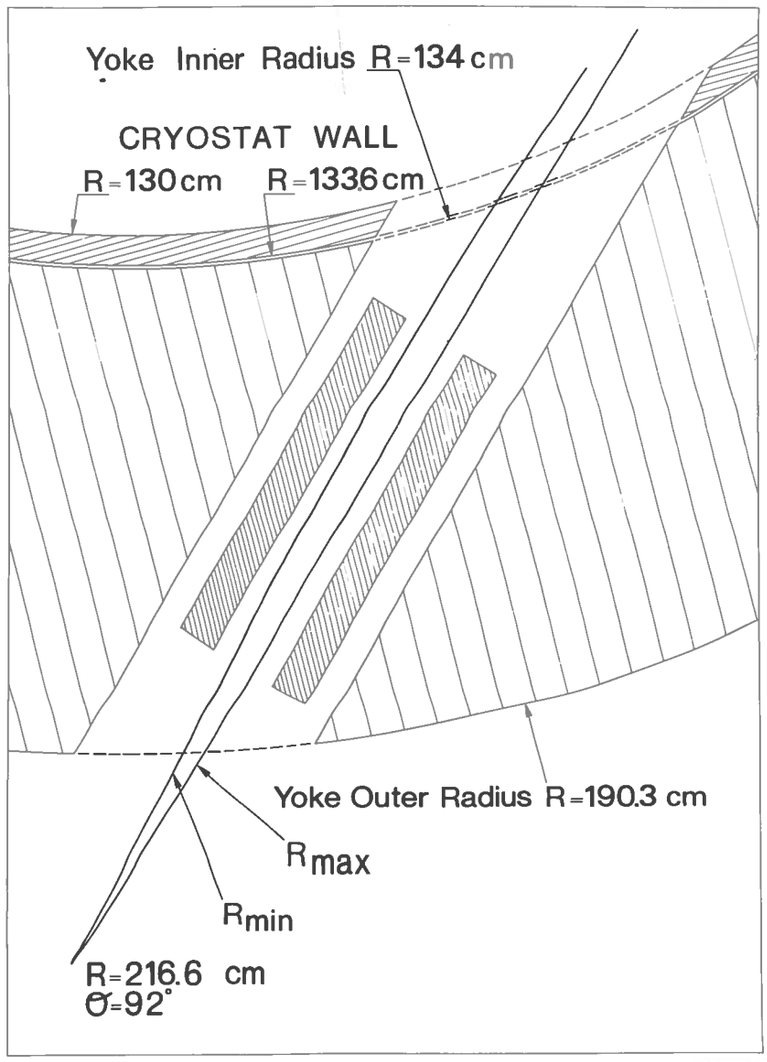

Fig. 21 - Schematical view of the envelope of all the central rays trajectories as they cross the yoke and through the magnetic channel M8. Shown is also the common exit point of all the beams.

at $\Theta = 68°$, azimuth close to the beam entrance into the yoke, at $\Theta = 88°$, azimuth close to the exit from the yoke and at the common point, $\Theta = 92°$. For further reference the appendix presents two (R,Θ) tables: the Table A1 giving every two degrees the minimum and the maximum radii of all the central rays trajectories and the Table A2 listing, again every two degrees, the central rays trajectories of all the ions chosen along the borders of the cyclotron operating diagram. The inner radii of the compensating bars C1a, C1b and C2 are listed for all the investigated ions in Table VI.

Table VII summarizes for all the beams the necessary electric fields of E1 and E2, the radius at the common exit point, $\Theta = 92°$, and the angle α at this position which is $63.34° \pm 2.43°$. This table shows, as expected, that the highest electric fields, i.e. E larger than 120 KV/cm, are required for the extraction of the ions close to the crossing between the bending and the focusing lines (the ions 0.3/41.4 and 0.25/45.5) and for the more relativistic ions, i.e. the ions 0.5/31.3 and 0.5/26.5.

Table VI. -
Compensating bars settings for the ions selected for this study

Z/A	B_o (kgauss)	C1a-C1b (cm)	C2 (cm)
0.5	31.3	91.90	97.60
	26.5	96.00	100.50
	22.0	95.90	99.90
0.4	22.0	96.40	101.30
0.3	41.4	93.00	98.10
	22.0	96.00	102.00
0.25	45.5	93.00	97.80
	40.0	92.90	97.80
	38.0	96.20	97.80
	30.0	95.80	99.00
0.1	47.5	92.90	97.70
	25.0	95.90	101.00

Table VII. - Electric fields and central ray data at $\Theta = 92°$

Z/A	B_o (kG)	T/A (MeV/n)	E (KV/cm)	R(Θ=92°) (cm)	α (deg)
0.5	31.3	100.50	135.37	216.60	62.14
	26.5	67.18	128.42	216.62	61.45
	22.0	44.01	75.65	216.61	61.08
0.4	22.0	27.59	42.55	216.59	61.05
0.3	41.4	59.63	139.69	216.59	65.02
0.25	45.5	49.42	123.98	216.60	65.58
	40.0	37.15	114.27	216.59	64.82
	38.0	33.23	102.97	216.60	63.81
	30.0	20.19	58.68	216.62	61.51
0.1	47.5	8.04	45.68	216.59	65.77
	25.0	2.10	17.77	216.61	60.91

The position of the central rays at $\Theta = 92°$ is extremely sensitive to variations of the electric field in E1 and E2. As an example, the displacement at $\Theta = 92°$ of the trajectories of two ions, namely the ions 0.3/41.4 and 0.5/22, is plotted as a function of a percentage variation of the electric field on E1 and E2 in Fig 22. The displacement dx is measured normal to the beam trajectory, as it could be seen on a beam probe. From the figure it is also apparent that any variation on the electric field of E1 is almost three

times more effecitve than an equal variation on E2. Fortunately the radial focusing effects of the magnetic channels reduce the displacements due to small variations of the electric fields by more than one order of magnitude. So the required stability of the power supplies of E1 and E2 can be of the order of 1/1000 in order to keep the beam position stable within 1 mm at the exit point.

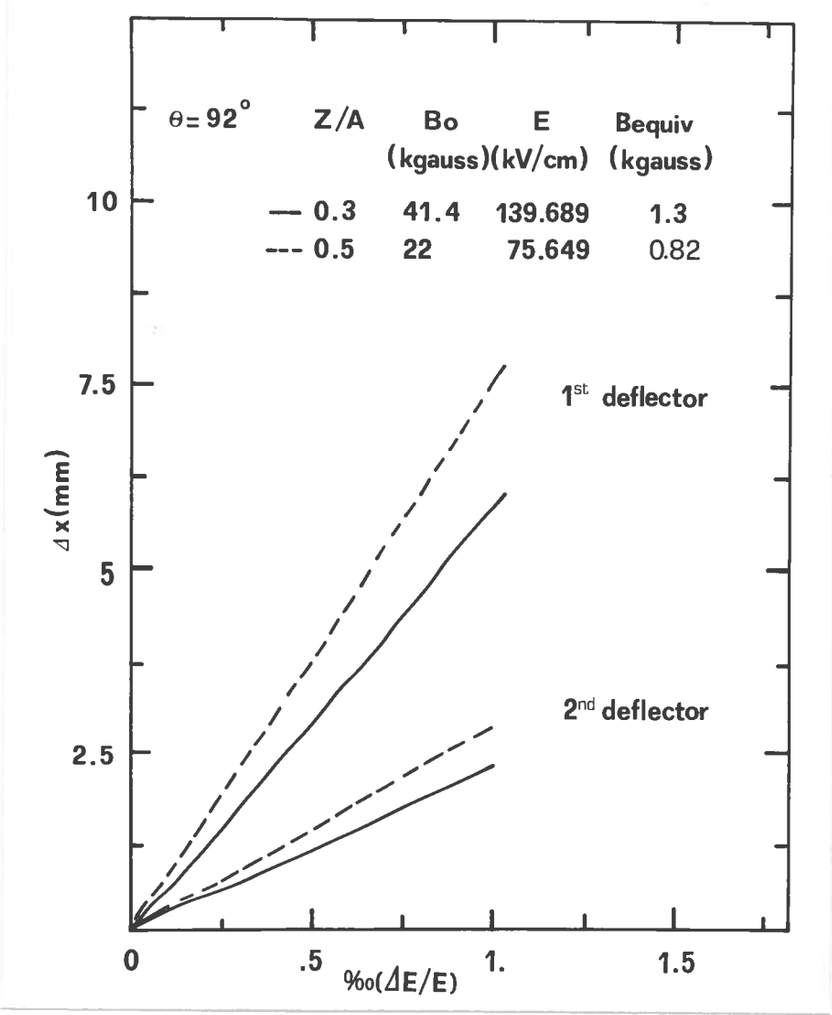

Fig. 22 - Displacement of the central rays trajectories at $\Theta = 92°$ plotted as a function of a percentage variation of the electric field on the electrostatic deflectors for the ions with $Z/A = 0.3$, $B_o = 41.4$ kgauss and $Z/A = 0.5$, $B_o = 22$ kgauss.

As previously stated the electric field is simulated with a field bias extending along the central ray trajectories from the initial deflector azimuth until the final azimuth, thus implying longer deflectors for the more external trajectories. This difference in the deflectors lengths turns out to be quite significant: it is around 1.2 cm for E1, which has an average length of 80 cm, and around 0.5 cm for E2, which has an average length of 63 cm. Let us recall that the length of the real deflectors is chosen on

the basis of the more internal trajectories in order to guarantee the necessary clearance between the dees and the deflectors themselves. Therefore an increase of the electric fields with respect to the values given in Table VII is necessary in order to keep the extraction trajectories along the designed extraction path. It has been checked that this increase will be of the order of 2-2.5% for the more relativistic ions as 0.5/31.3, 0.3/41.4 and 0.25/45.5.

The uncertainities on the B_{yoke} values do not pose serious problems concerning the proper centering of the beams at the exit point. In fact even assuming $B_{yoke} = 0$, so that there is no change in the curvature of the trajectories throughout the yoke, we checked that negligible changes in the deflectors electric field will be necessary. Changes are less than 1% even for the ion with Z/A = 0.3 and B_o = 41.4 kgauss for which a B_{yoke} = -4 kgauss was assumed.

It has been carefully checked on 1:1 drawings of the cyclotron median plane cross section that the extraction hardware will not interfere with the dees and the liner. A critical point is the position of the magnetic channel M2 which is very close to the dee, as shown in the vertical cross section at Θ = 282° of Fig. 23. In the figure the channel

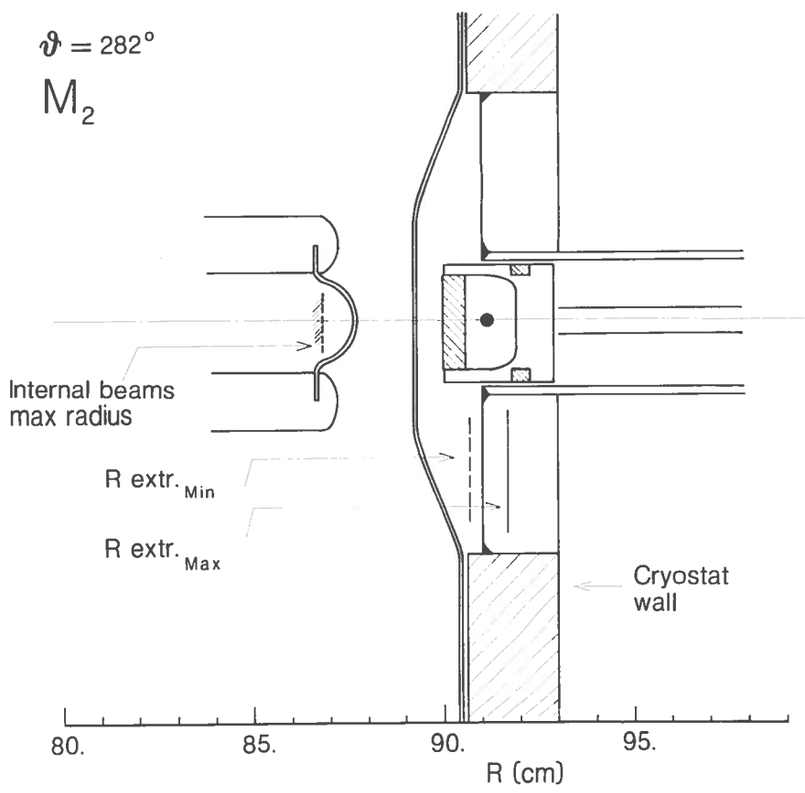

Fig. 23 - Vertical cross section of the magnetic channel M2 at Θ = 282° showing also the dee and the liner. The maximum radius of the envelope of all the internal beams, the minimum and maximum radii of the extraction trajectories are also indicated.

is shown as centered on the trajectory of the ion with Z/A = 0.1 and B_o = 47.5 kgauss, which is one of the more internally extracted beams requiring radial focusing immediately after M1. The maximum radius of the internal beams, the minimum and the maximum radii of the extracted trajectories are also indicated. Since the dee-liner clearance is reduced in this region to only 15 mm and since a further reduction is not possible, it has been decided to drill an extra hole from Θ = 296° to Θ = 304°. This is the region where the distance between the dee and the minimum radius of the extracted trajectories is larger than 38 mm and this hole could be used for the insertion of the channel M2. This if the extraction studies on the measured magnetic field maps shall indicate the need of this channel also for the more internal trajectories as those of the ions with B_o = 22 kgauss. It was checked that also with the latter solution a good phase space behaviour can been obtained for all the beams. However some change in the geometry of the bars C1a and C1b which compensate for the first harmonic field perturbation produced by M1 and M2[1] will be necessary. The more straightfor change will be simply to extend C1b from Θ = 158.85° to Θ = 162.81° instead of the present solution which calls for Θ_i = 158.85° and Θ_f = 161.0°.

3.3. - Phase space behaviour

The phase space behaviour through the extraction path has been investigated using as starting conditions at Θ = 100° the accelerated beams obtained as reported in Ref. 1. For each charge to mass ratio the emittances of the beams were assumed to be around 5 mm·mrad in both the radial and axial phase spaces for the maximum energies and around 7 mm·mrad for the minimum energies.

The beam envelopes along the extraction path are shown for the ions on the borders of the cyclotron operating diagram in Figs. 24-31, where the x coordinate is the maximum radial width of the beam perpendicular to the central ray direction and the z coordinate is the maximum axial half-width. It is apparent from the figures that all the beams are well confined in both spaces never being larger than ±4 mm at least up to Θ = 68°, an azimuth close to the exit from the cryostat. In particular one can note that:

- The beams are usually less than 4 mm wide inside the electrostatic deflectors. The only exceptions are the low field ions, as the 0.4/22 and the 0.3/22 which are about 6 mm wide at the exit from the 2nd electrostatic deflector. This however should not pose serious problems for the extraction efficiency since, we espect to center all the beams

inside E2 within ±0.5 mm.

- All the beams require a magnetic channel immediately after E2.
- The number of magnetic channels used for the different beams depends on the main field level. All channels from M1 to M7 are required at high field levels, i.e. from the maximum B_o = 47.5 kgauss down to field levels around 38-40 kgauss. At lower field levels M2 must be removed, since otherwise a radial overfocusing of the beams is produced. No clear pattern emerges about which of the other following channels (M3 to M7) must be removed, because this dependents strongly on both the beam starting conditions and the field level. The necessary configuration of the magnetic channels is given in Table VIII for all the investigated ions. For one ion, namely the 0.3/41.4 ion, even the complete set of magnetic channels seems not to be sufficient, since the beam has a radial width of about ±4 mm with a maximum divergence of 5 mrad while entering the yoke. However, if the channel $M7_{bis}$ (from Θ = 50° to Θ = 56°) is used this radial width is reduced to ±3 mm and, moreover, the radial divergence is reduced to one half.

Table VIII. -
Magnetic channel settings for the ions selected for this study

Z/A	B_o	M1	M2	M3	M4	M5	M6	M7
0.5	31.3							
	26.5	yes	-	yes	-	yes	yes	yes
	22.0	yes	-	yes	yes	-	-	yes
0.4	22.0	yes	-	-	yes	yes	yes	-
0.3	41.4	yes	yes	yes	yes	yes	yes	yes
	22.0	yes	-	-	-	yes	yes	-
0.25	45.5	yes	yes	yes	yes	yes	yes	yes
	40.0	yes	yes	yes	yes	yes	yes	yes
	38.0	yes	-	yes	yes	yes	yes	yes
	30.0	yes	-	yes	yes	-	yes	yes
0.1	47.5	yes	yes	yes	yes	yes	yes	yes
	25.0	yes	-	-	yes	yes	yes	-

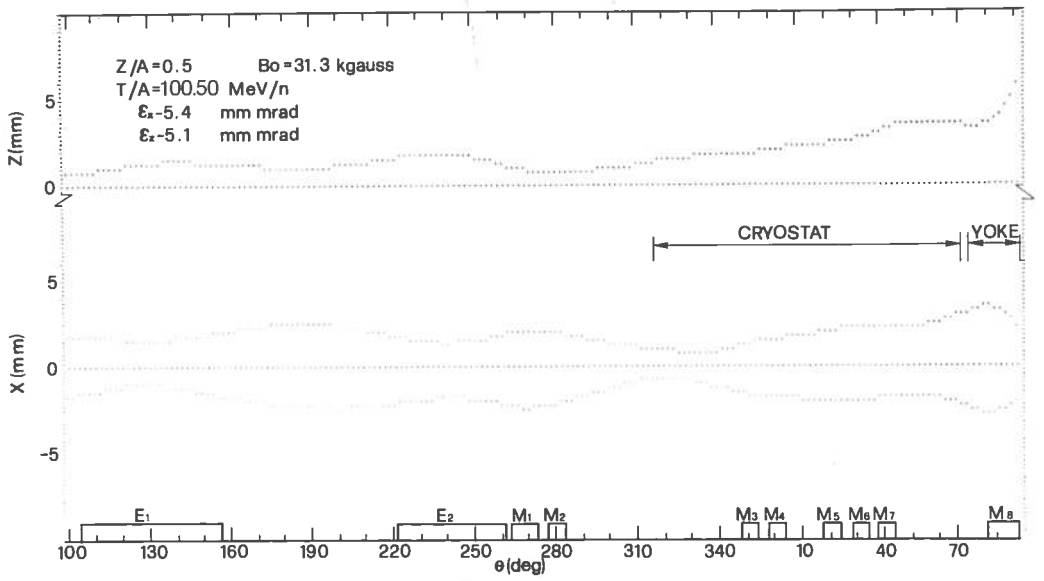

Fig. 24 - Radial and axial beam envelopes along the extraction path for the ion 0.5/31.3

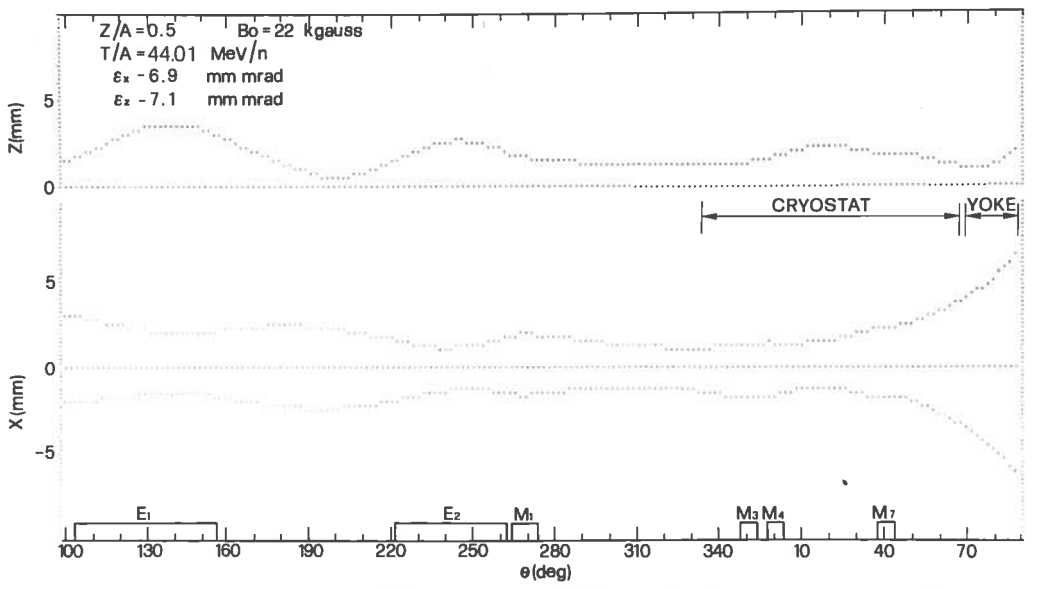

Fig. 25 - Radial and axial beam envelopes along the extraction path for the ion 0.5/22

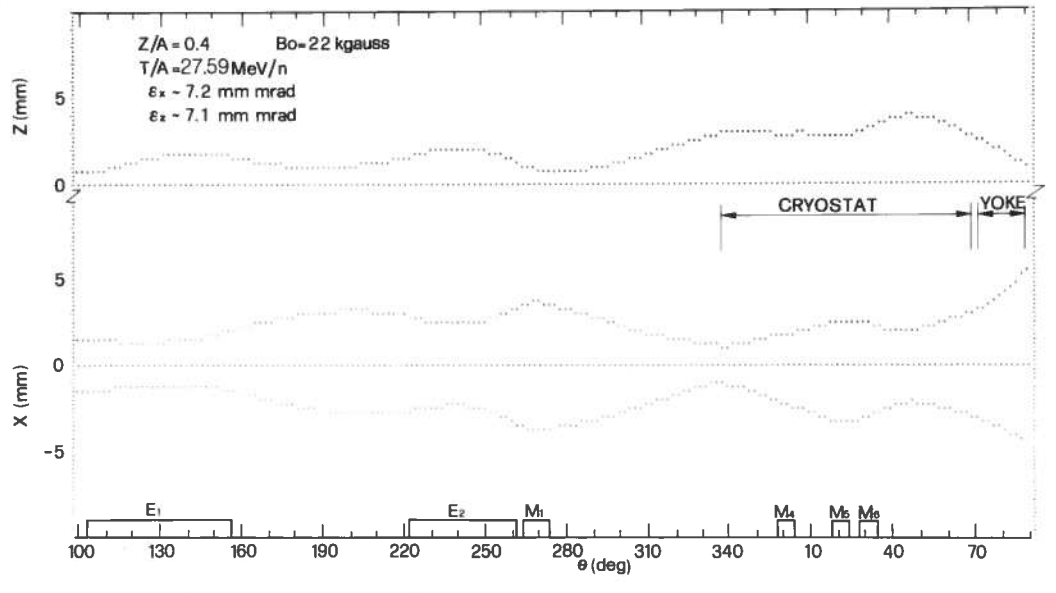

Fig. 26 - Radial and axial beam envelopes along the extraction path for the ion 0.4/22.2

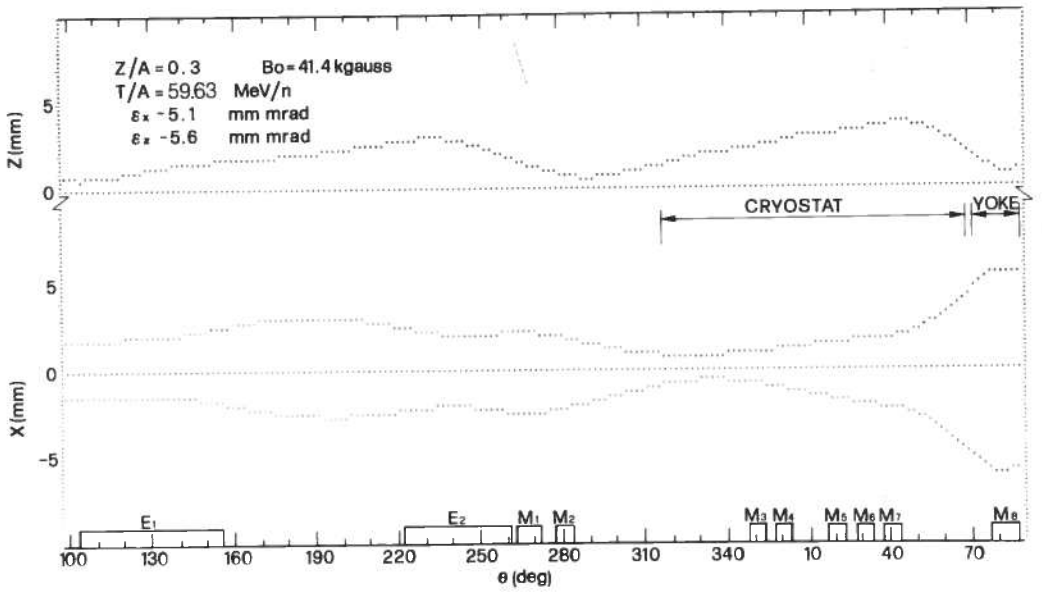

Fig. 27 - Radial and axial beam envelopes along the extraction path for the ion 0.3/41.4

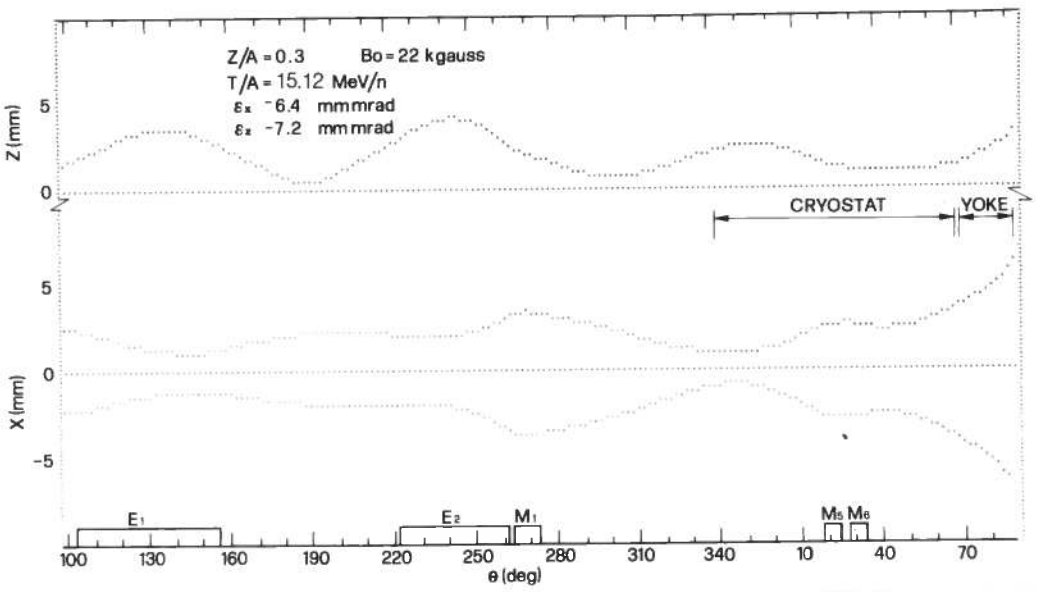

Fig. 28 - Radial and axial beam envelopes along the extraction path for the ion 0.3/22

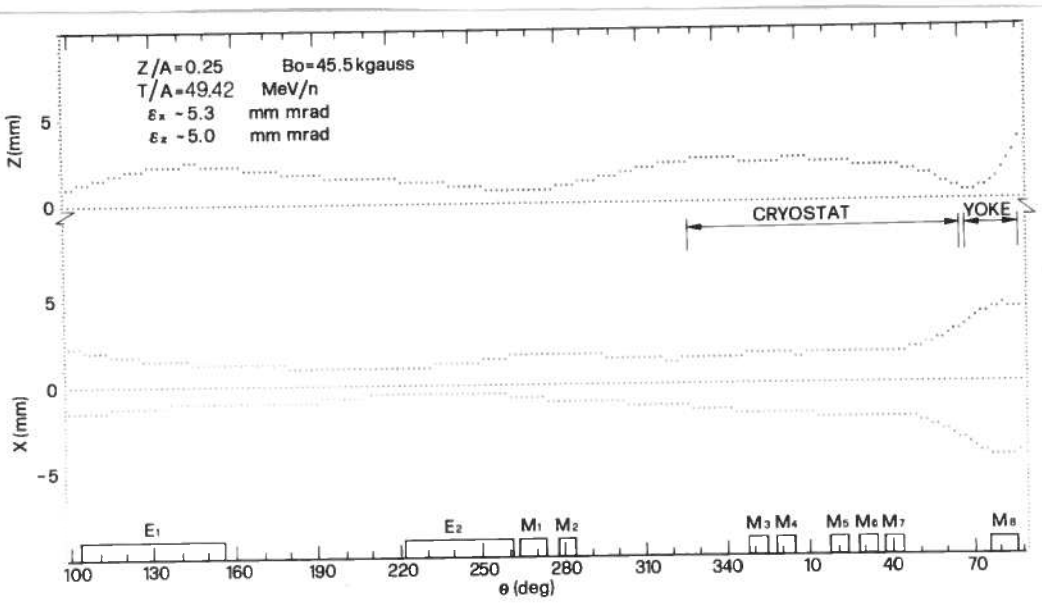

Fig. 29 - Radial and axial beam envelopes along the extraction path for the ion 0.25/45.5

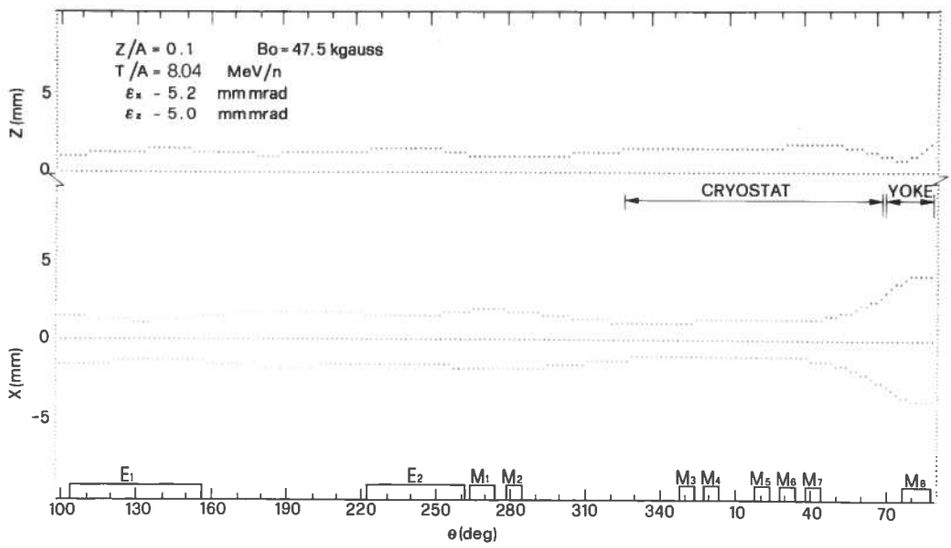

Fig. 30 - Radial and axial beam envelopes along the extraction path for the ion 0.1/47.5

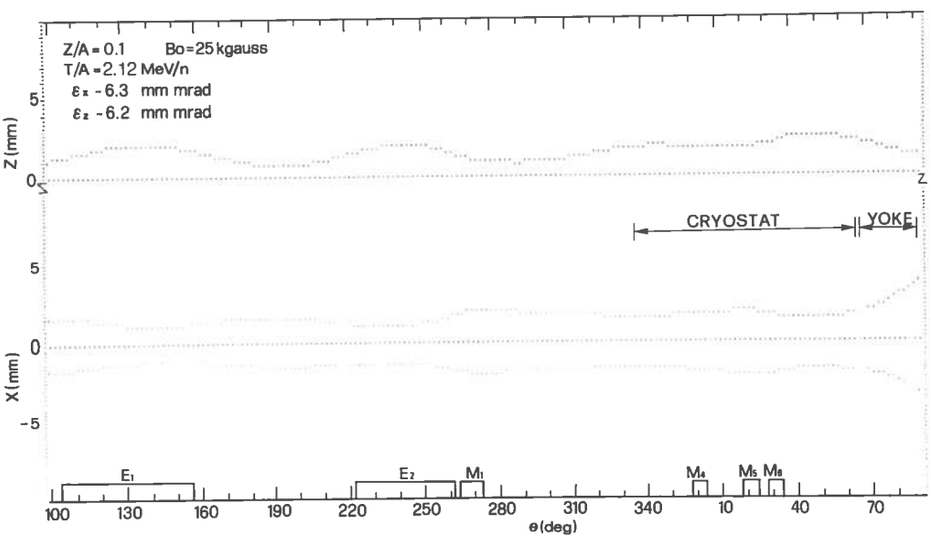

Fig. 31 - Radial and axial beam envelopes along the extraction path for the ion 0.1/25

The radial and axial phase space at the entrance of the yoke, namely at the azimuth $\Theta = 68°$ where all the ions have a radius close to 130 cm, are shown in Fig. 32 for the ions 0.1/47.5, 0.25/45.5, 0.3/41.4 and 0.5/31.3 and in Fig. 33 for the ions 0.1/25, 0.5/22, 0.4/22 and 0.3/22. Although the beams radial dimensions are confined within ± 5 mm or mrad all the beams are strongly defocused at this position with a divergence almost equal to the beam width. In the axial plane instead all the beams are generally focused although with different positions depending on the ion and the field.

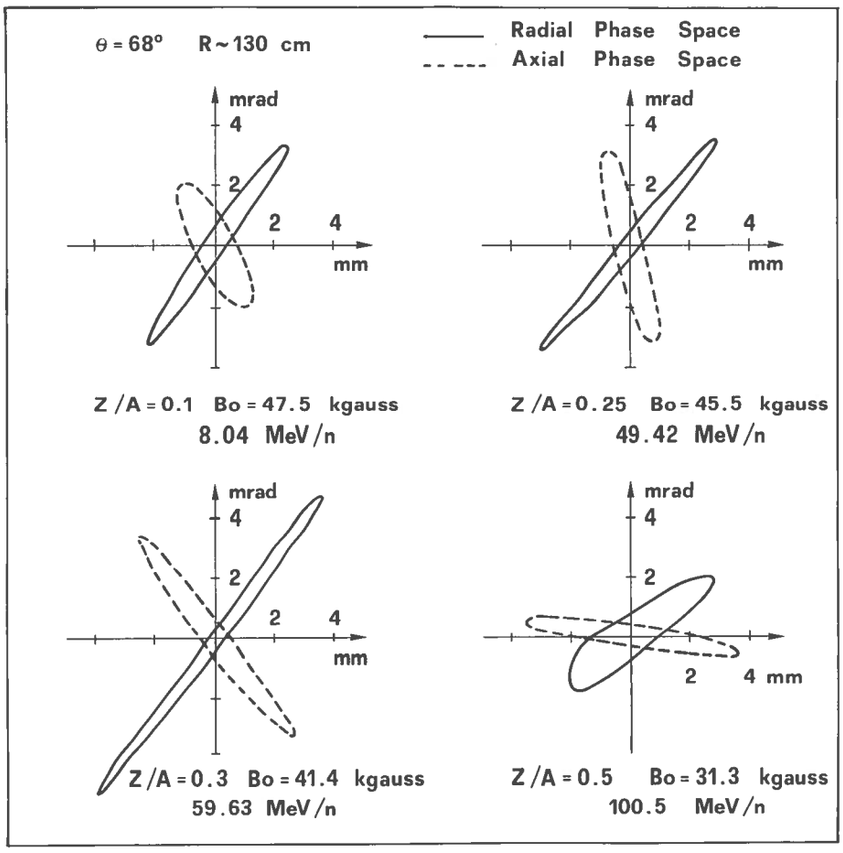

Fig. 32 - Radial and axial phase spaces at the exit from the cryostat (Θ = 68°, R ~ 130cm) for four ions extracted at their maximum field level.

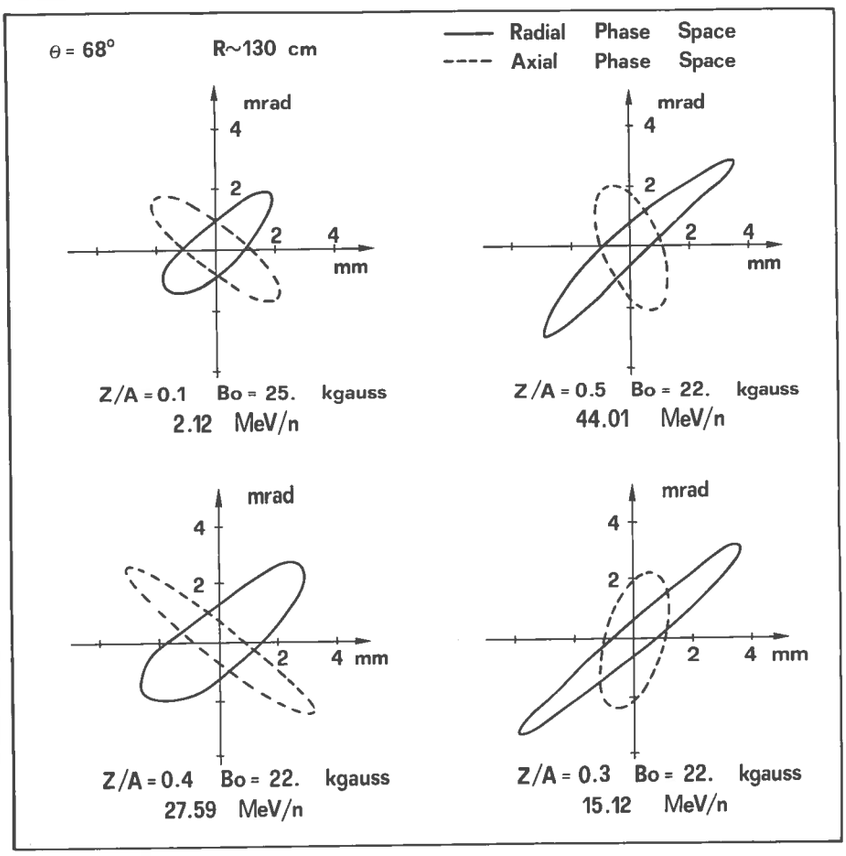

Fig. 33 - Radial and axial phase spaces at the exit from the cryostat (Θ = 68°, R ~ 130cm) for four ions extracted at a low field level.

Since the yoke traversal is 80 cm long there will be a non trivial radial enlargement of the beams. In fact at Θ = 92°, R = 216 cm where all the trajectories meet outside the machine almost all the ions have doubled their beam radial width with respect to the Θ = 68° azimuth as shown by the radial and axial phase spaces presented in Figs. 34 and 35. Both the beams radial width and divergence can be reduced with the use of a magnetic channel acting during the yoke traversal. The field gradient of the passive magnetic channel M8 (Fig. 9) has been chosen in order to obtain beams almost parallel in the radial phase space at the Θ = 92° azimuth, being this phase space configuration convenient for the successive beam handling. The radial and axial phase spaces obtained for the high field ions at Θ = 92° with the use of the channel M8 are shown in Fig. 36. Obviously a magnetic channel of the passive type will not be effective for the low field ions. Thus it will be necessary to use an active channel in order to obtain also for these ions beams almost parallel in the radial phase space. We have verified that a field gradient in the channel of 0.25 kgauss/cm is enough as it can be seen in Fig. 37 showing the radial and axial phase space obtained in these case at Θ = 92°.

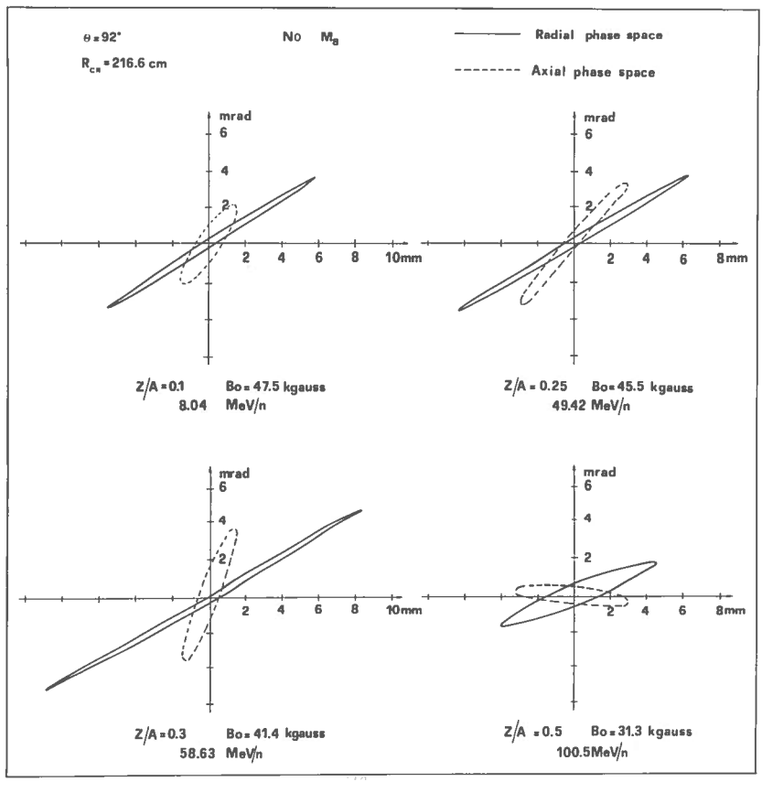

Fig. 34 - Radial and axial phase spaces at the exit point for four ions extracted at their maximum field level. No magnetic channel is assumed in the yoke traversal.

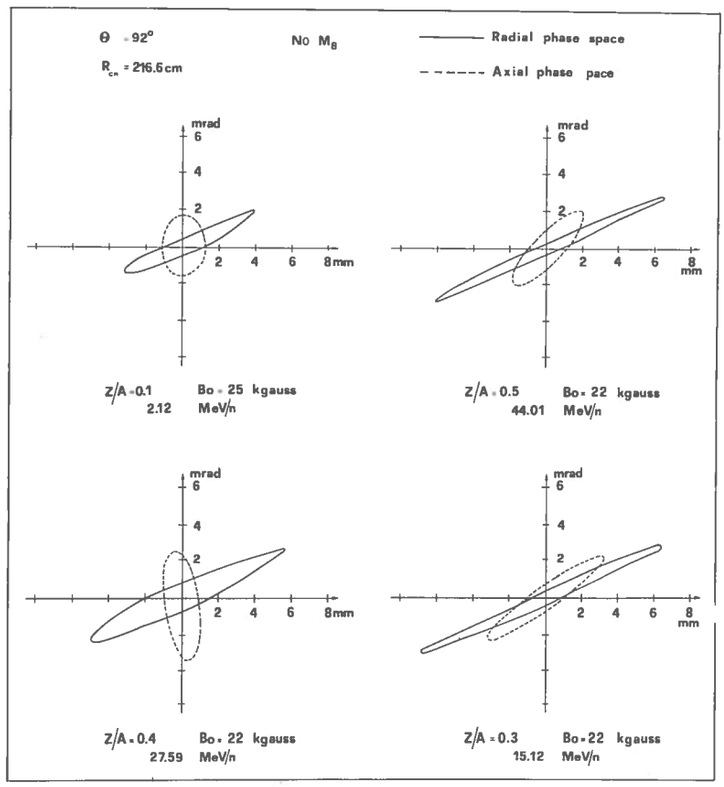

Fig. 35 - Radial and axial phase spaces at the exit point for four ions extracted at a low field level. No magnetic channel is assumed in the yoke traversal.

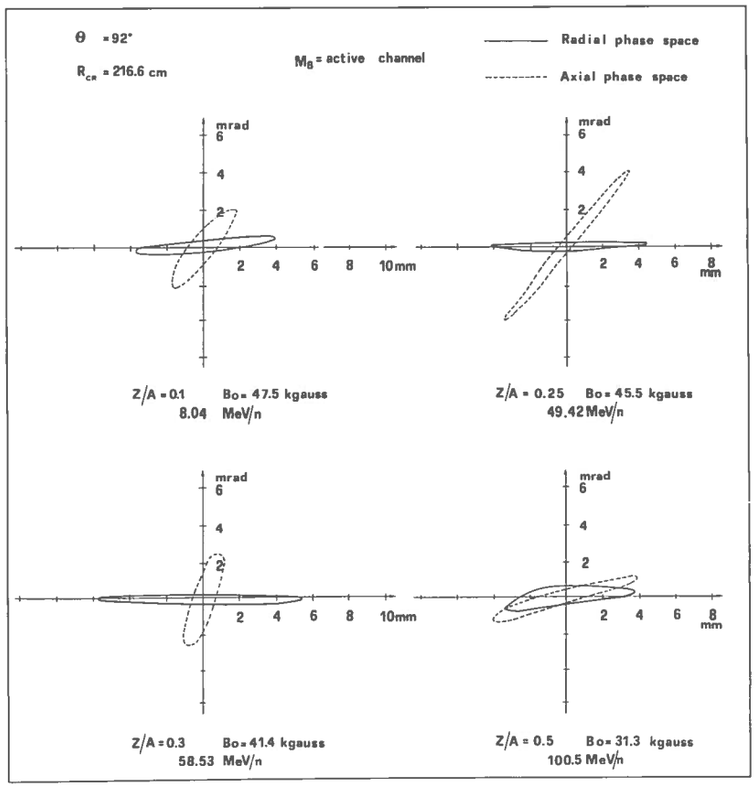

Fig. 36 - Radial and axial phase spaces at the exit point four ions extracted at their maximum field level when the magnetic channel M8 is used.

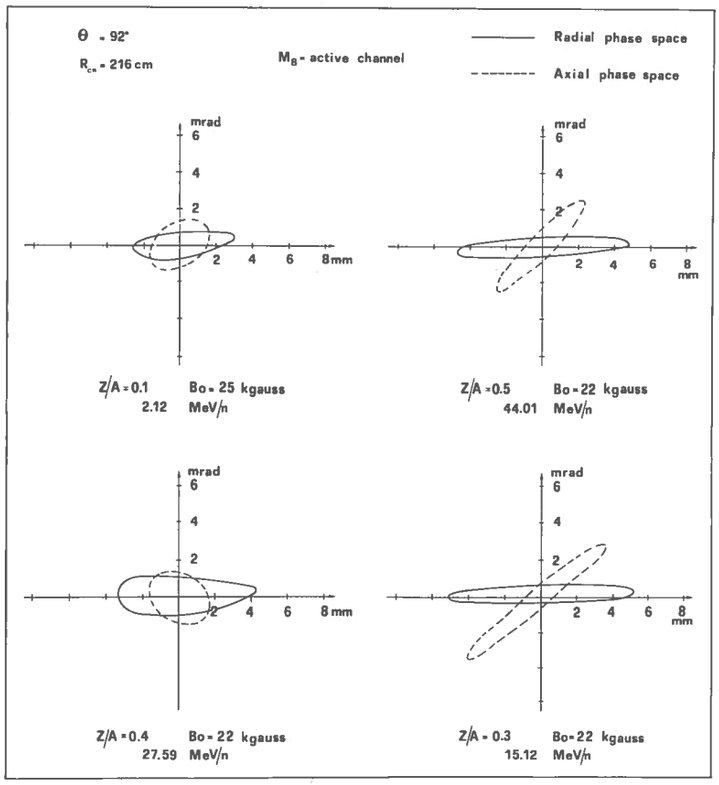

Fig. 37 - Radial and axial phase spaces at the exit point for four ions extracted at a low field level when an active magnetic channel is used in the yoke traversal. A field gradient of 0.25 kgauss/cm has been assumed.

3.4. - Dispersive effects

The radial and angular dispersion due to an energy spread in the extracted beam must be known in order to design the beam transport line. The dispersive effects were investigated assuming a possible energy spread $\Delta E/E = \pm 0.1\%$ at the entrance of the 1st electrostatic deflector and consequentely "dispersed central rays" for all the investigated ions have been tracked along the extraction path. These rays have the same radial coordinates at $\Theta = 100°$ as determined by the beam dynamics calculations summarized in Table VI, while their energies and momenta are varied according to the assumed energy spread. In the following the radial and angular dispersions of these central rays, averaged between the two cases $\Delta E/E = -0.1\%$ and $\Delta E/E = +0.1\%$ are quoted respectively as R_{16} and R_{26} and, consistently with the conventions of the beam transport code TRANSPORT[12], they are given in cm per percent of momentum variation (R_{16}) and mrad per percent of momentum variation (R_{26}).

These dispersive effects are not negligible especially for high field ions. For the latter the radial dispersions double during the yoke traversal if the magnetic channel M8 is not used. This can be seen in Fig. 38 where the dispersed central rays are plotted in the (x,p_x) space at $\Theta = 68°$, near the exit from the cryostat, and at the common point outside the cyclotron, $\Theta = 92°$. The radial and angular dispersions at $\Theta = 92°$ are summarized in the (R_{16},R_{26}) space in Fig. 39 for all ions along the borders of the the cyclotron operating diagram, always assuming no magnetic channel during the yoke traversal. In fact a magnetic channel acting during the yoke traversal is quite effective in reducing the angular dispersion as shown in Fig. 40 where the R_{26} parameter at $\Theta = 90°$ and R = 216.60 cm is plotted for different ions as a function of the focusing gradient of the magnetic channel in the yoke traversal. Similarly the Fig. 41 shows the R_{16} dependence

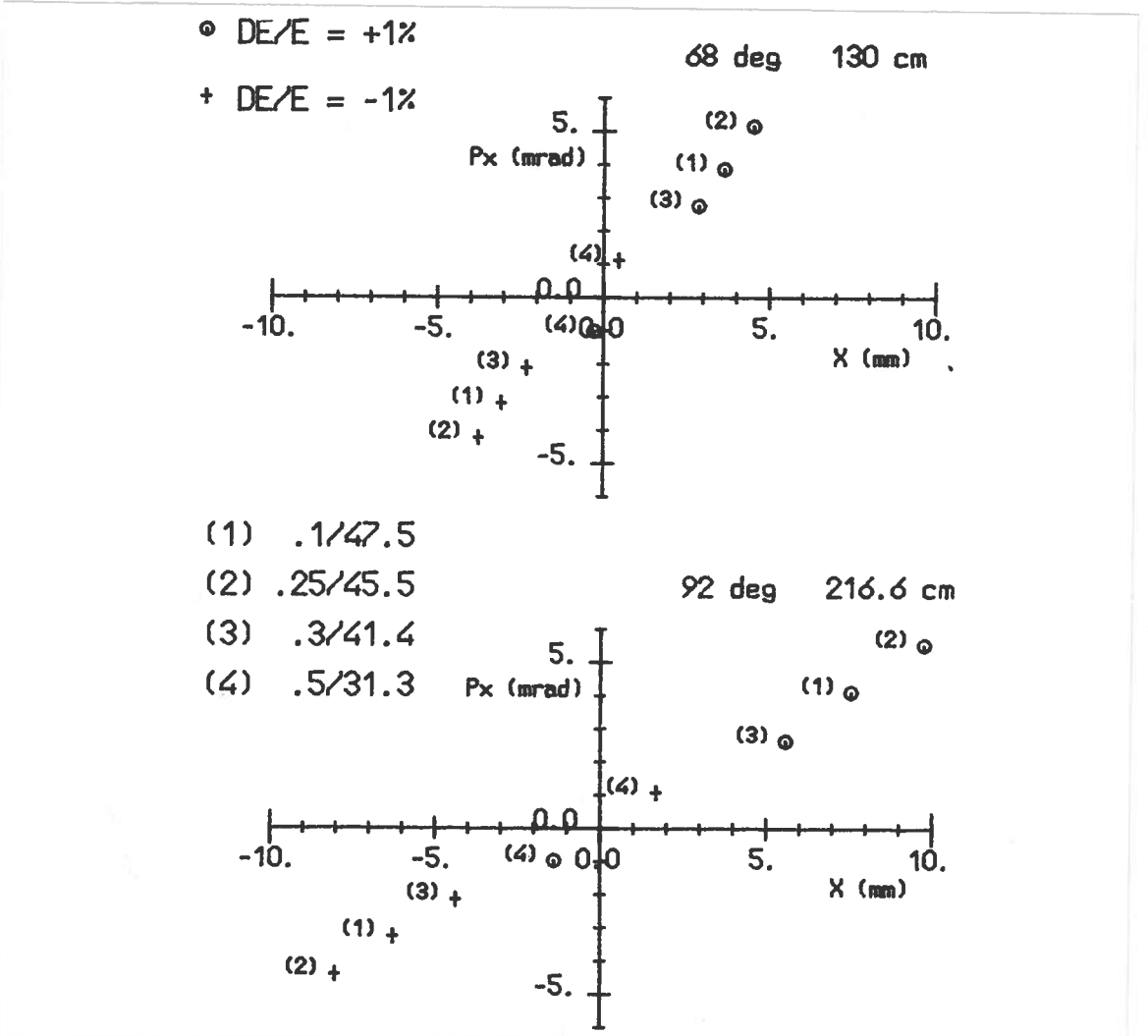

Fig. 38 - Central rays with an energy dispersion of $\Delta E/E = \pm 0.1\%$ plotted in the phase space (x,p_x) at $\Theta = 68°$ and at $\Theta = 92°$ for four ions extracted at the maximum field level. No magnetic channel is assumed in the yoke traversal.

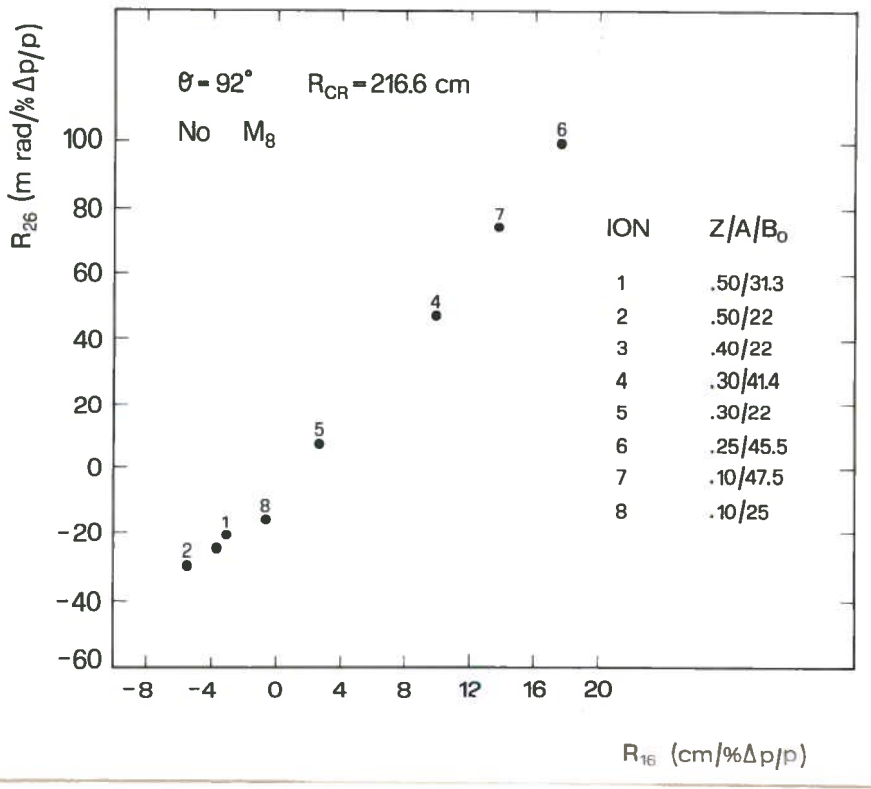

Fig. 39 - Dispersive effects in term of radial dispersion (R_{16}) and angular dispersion (R_{26}) for the ions chosen along the borders of the cyclotron operating diagram. No magnetic channel is assumed in the yoke traversal.

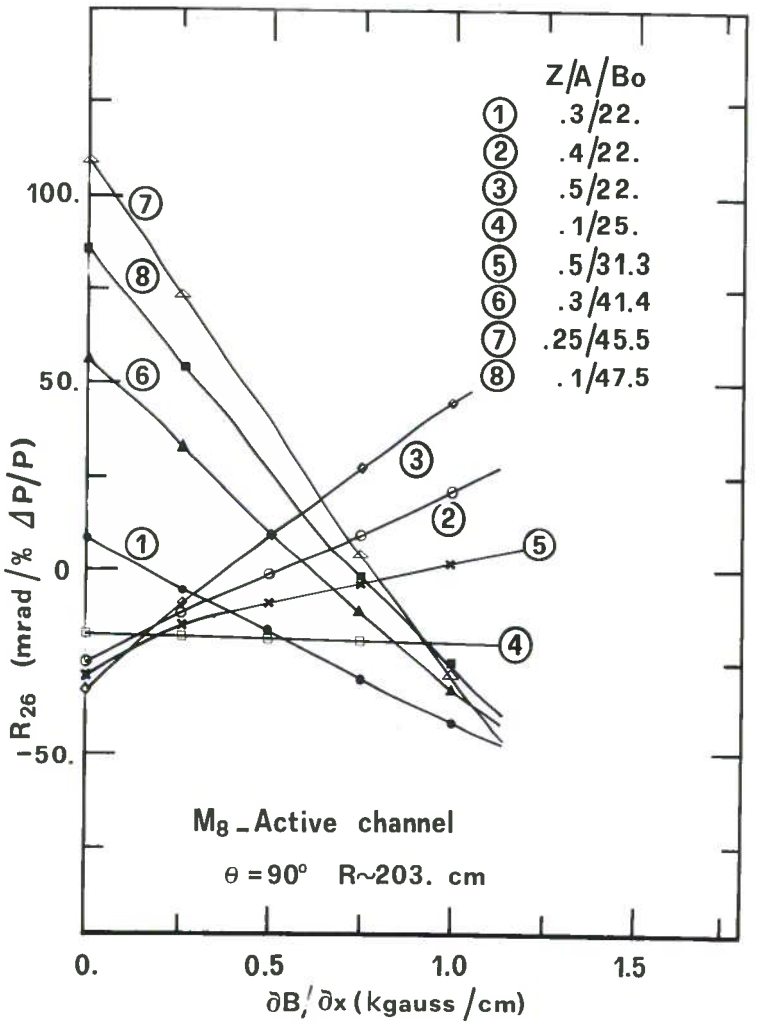

Fig. 40 - Angular dispersion at Θ = 90° plotted as a function of the focusing gradient of the magnetic channel in the yoke traversal for the eight ions chosen along the borders of the cyclotron operating diagram.

from the channel's field gradient.

The R_{16} and R_{26} parameters obtained at $\Theta = 92°$, R = 216.6 cm using the passive channel M8 are shown in Fig. 42 and summarised in Table IX. The angular divergency of the high field beams is in this way drastically reduced. As an example, for the ion 0.25/45.5 the R_{26} parameter, which is around 100 mrad/(%Δp/p) without the use of M8, goes down to 2 mrad/(%Δp/p). The passive channel is not effective at low field levels, but, due to the limited dispersive effects exhibited by the beams accelerated at these fields, the use of a magnetic channel is not required. For the sake of completeness the results obtained in the (R_{16},R_{26}) space using an active channel are shown in Fig. 43. For the low field ions we selected the same focusing gradient in the yoke channel (0.25 kgauss/cm) as assumed previously in tracking the phase spaces presented in Fig.37.

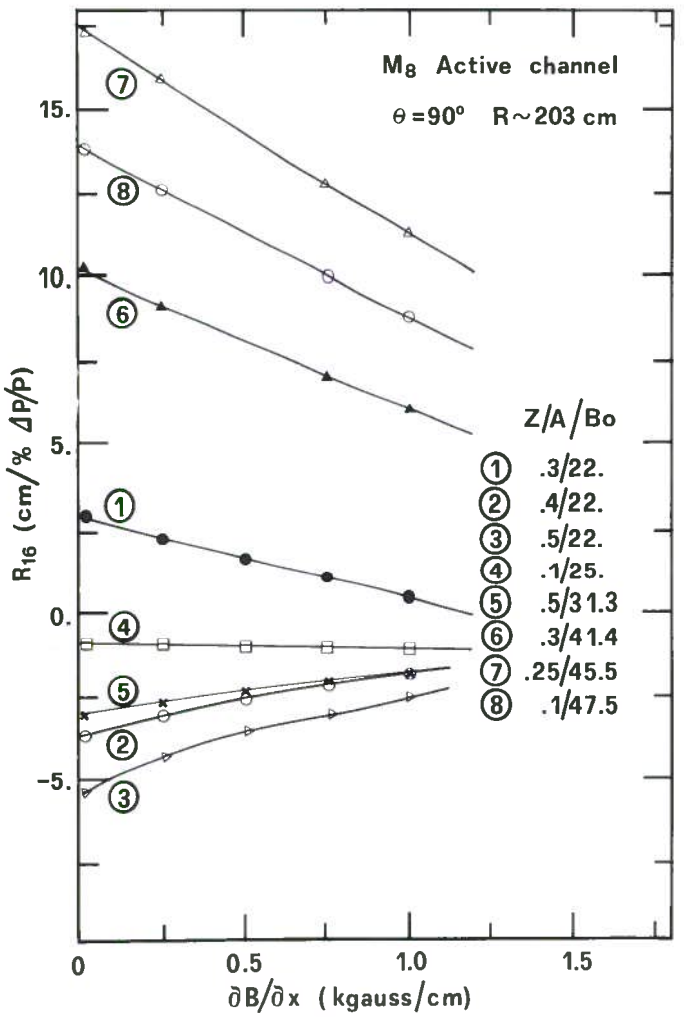

Fig. 41 - Radial dispersion at $\Theta = 90°$ plotted as a function of the focusing gradient of the magnetic channel in the yoke traversal for the eight ions chosen along the borders of the cyclotron operating diagram.

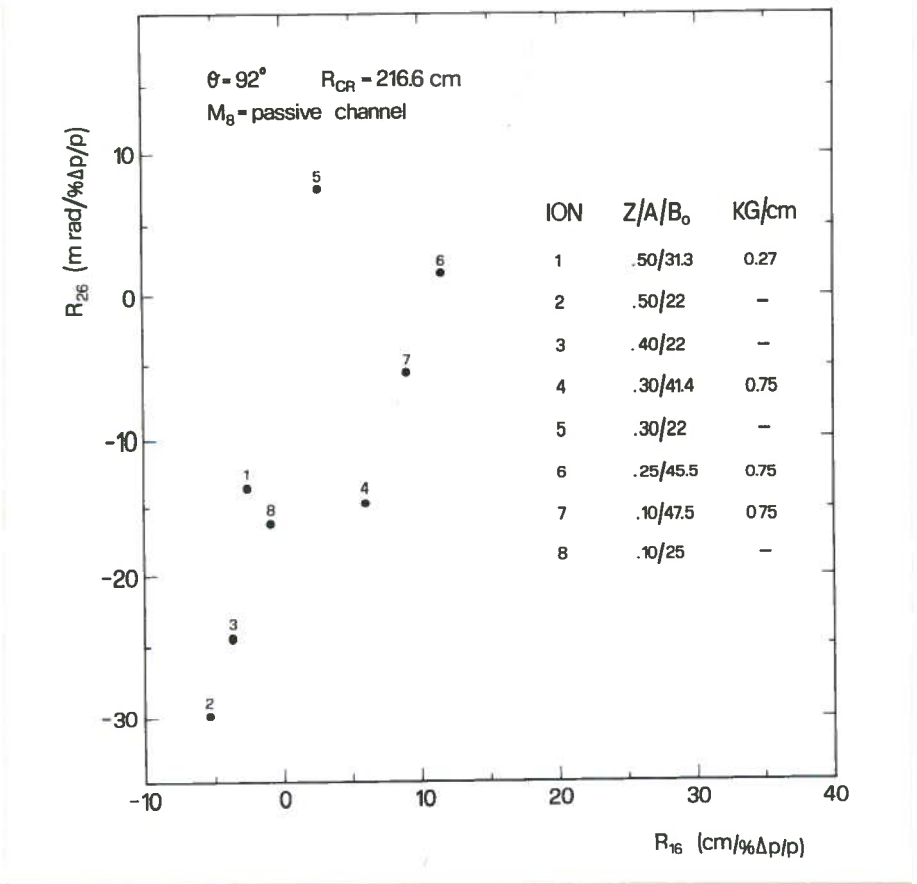

Fig. 42 - Dispersive effects in term of radial dispersion (R_{16}) and angular dispersion (R_{26}) for the ions chosen along the borders of the cyclotron operating diagram when the passive magnetic channel M8 is used in the yoke traversal. The field gradients assumed inside the channel are indicated.

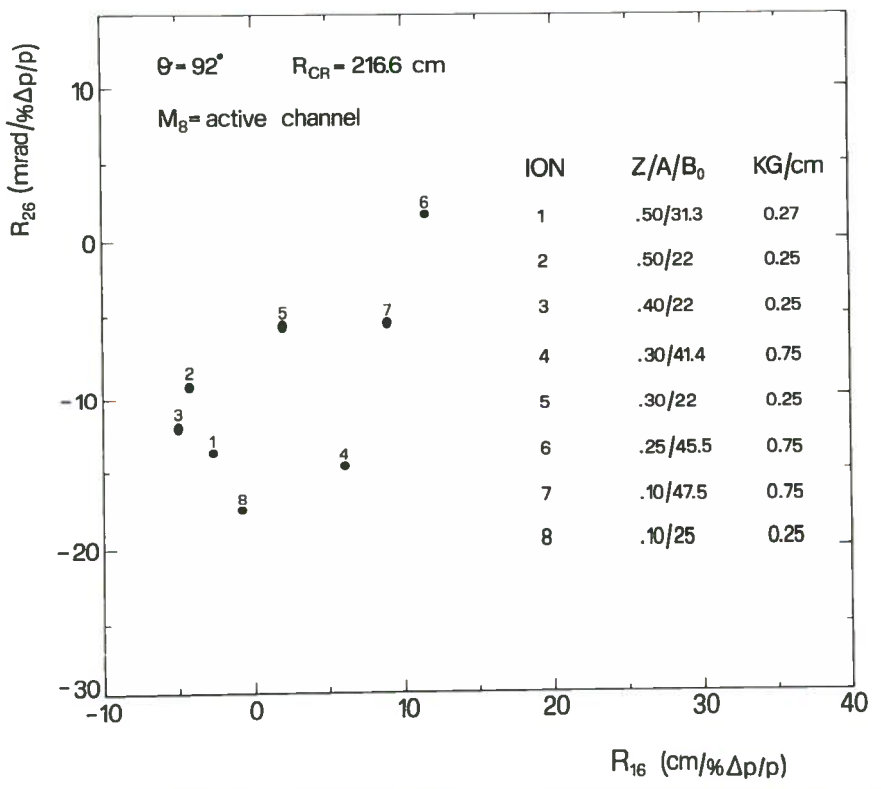

Fig. 43 - Dispersive effects in term of radial dispersion (R_{16}) and angular dispersion (R_{26}) for the ions chosen along the borders of the cyclotron operating diagram when an active magnetic channel is used in the yoke traversal. The field gradients inside the channel are indicated.

Table IX. - Central ray data and dispersions at $\Theta = 92°$

Z/A	B_o kG	R cm	P Mev/c	α deg	R_{16} cm/(%∂p/p)	R_{26} mrad/(%∂p/p)
0.5	31.3	216.60	444.2257	62.14	-2.6494	-13.5850
	22.0	216.61	289.6852	61.08	-5.4326	-29.5160
0.4	22.0	216.59	228.3954	61.05	-3.7254	-24.6100
0.3	41.4	216.59	338.5912	65.02	+6.0460	-14.6500
	22.0	216.59	168.5028	60.99	+2.7160	+7.3520
0.25	45.5	216.60	307.4121	65.58	+11.6082	+1.7000
0.1	47.5	216.59	122.6658	65.77	+8.9542	-5.5390
	25.0	216.61	62.9489	60.91	-0.6820	-16.1020

4. - CONCLUSIONS

The extraction system presented here is based on a quite extensive analysis of the beams dynamics before extraction and along the extraction path and it looks fully capable of meeting the design requirements. Obviously these calculations will be checked with the measured magnetic field maps when they will be available.

The major uncertainities are on the fringing field, which is crucial for the beams optics. An other point to be checked is the possibility to hold stably an electric field of 140 KV/cm on the electrostatic deflectors. If this should not be the case we can, possibly, increase the field bias of the magnetic channels. Calculations of the new channels geometry and of the necessary compensations are now in progress.

Table A1. - Minimum and maximum radii of the extraction trajectories

	Θ (deg)	Rmin (cm)	Rmax (cm)		Θ (deg)	Rmin (cm)	Rmax (cm)
	100.0	83.749	86.782		218.0	86.640	89.002
	102.0	84.088	86.929		220.0	86.955	89.138
E1	104.0	84.442	87.080	E2	222.0	87.282	89.277
E1	106.0	84.781	87.230	E2	224.0	87.613	89.417
E1	108.0	85.123	87.380	E2	226.0	87.942	89.578
E1	110.0	85.460	87.582	E2	228.0	88.260	89.750
E1	112.0	85.787	87.775	E2	230.0	88.563	89.916
E1	114.0	86.097	87.955	E2	232.0	88.849	90.074
E1	116.0	86.386	88.123	E2	234.0	89.117	90.224
E1	118.0	86.653	88.277	E2	236.0	89.365	90.364
E1	120.0	86.896	88.416	E2	238.0	89.594	90.496
E1	122.0	87.113	88.540	E2	240.0	89.804	90.620
E1	124.0	87.304	88.650	E2	242.0	89.979	90.734
E1	126.0	87.469	88.744	E2	244.0	90.133	90.840
E1	128.0	87.608	88.823	E2	246.0	90.245	90.937
E1	130.0	87.720	88.887	E2	248.0	90.339	91.026
E1	132.0	87.805	88.936	E2	250.0	90.425	91.107
E1	134.0	87.864	88.969	E2	252.0	90.506	91.179
E1	136.0	87.896	88.987	E2	254.0	90.580	91.244
E1	138.0	87.901	88.989	E2	256.0	90.648	91.301
E1	140.0	87.879	88.976	E2	258.0	90.709	91.350
E1	142.0	87.830	88.948	E2	260.0	90.765	91.393
E1	144.0	87.754	88.904	E2	262.0	90.815	91.427
E1	146.0	87.651	88.844		264.0	90.844	91.453
E1	148.0	87.520	88.769	M1	266.0	90.837	91.472
E1	150.0	87.363	88.678	M1	268.0	90.822	91.490
E1	152.0	87.180	88.573	M1	270.0	90.799	91.506
E1	154.0	86.979	88.458	M1	272.0	90.771	91.520
E1	156.0	86.769	88.341	M1	274.0	90.740	91.533
	158.0	86.556	88.224		276.0	90.710	91.546
	160.0	86.345	88.146		278.0	90.679	91.569
	162.0	86.108	88.082	M2	280.0	90.650	91.605
	164.0	85.874	88.023	M2	282.0	90.626	91.647
	166.0	85.652	87.968	M2	284.0	90.607	91.696
	168.0	85.444	87.919		286.0	90.595	91.751
	170.0	85.252	87.876		288.0	90.590	91.809
	172.0	85.076	87.840		290.0	90.592	91.870
	174.0	84.918	87.810		292.0	90.602	91.934
	176.0	84.778	87.788		294.0	90.620	92.002
	178.0	84.658	87.772		296.0	90.647	92.073
	180.0	84.557	87.764		298.0	90.682	92.148
	182.0	84.477	87.763		300.0	90.725	92.226
	184.0	84.417	87.769		302.0	90.777	92.308
	186.0	84.378	87.783		304.0	90.829	92.394
	188.0	84.360	87.804		306.0	90.891	92.484
	190.0	84.363	87.832		308.0	90.961	92.577
	192.0	84.388	87.868		310.0	91.039	92.674
	194.0	84.433	87.912		312.0	91.126	92.775
	196.0	84.500	87.963		314.0	91.221	92.880
	198.0	84.589	88.021		316.0	91.324	92.988
	200.0	84.699	88.086		318.0	91.437	93.101
	202.0	84.830	88.159		320.0	91.557	93.219
	204.0	84.983	88.240		322.0	91.686	93.340
	206.0	85.157	88.327		324.0	91.824	93.466
	208.0	85.353	88.422		326.0	91.971	93.597
	210.0	85.569	88.524		328.0	92.126	93.733
	212.0	85.806	88.633		330.0	92.290	93.873
	214.0	86.064	88.749		332.0	92.464	94.020
	216.0	86.342	88.872		334.0	92.647	94.172

	Θ (deg)	Rmin (cm)	Rmax (cm)
	336.0	92.840	94.329
	338.0	93.042	94.493
	340.0	93.253	94.663
	342.0	93.467	94.839
	344.0	93.684	95.020
	346.0	93.905	95.207
M3	348.0	94.130	95.399
M3	350.0	94.359	95.599
M3	352.0	94.592	95.808
M3	354.0	94.831	96.026
	356.0	95.075	96.253
M4	358.0	95.325	96.488
M4	.0	95.587	96.733
M4	2.0	95.864	96.989
M4	4.0	96.158	97.259
	6.0	96.467	97.542
	8.0	96.789	97.835
	10.0	97.124	98.141
	12.0	97.474	98.461
	14.0	97.841	98.795
	16.0	98.227	99.145
M5	18.0	98.633	99.521
M5	20.0	99.066	99.925
M5	22.0	99.531	100.356
M5	24.0	100.030	100.817
	26.0	100.563	101.308
M6	28.0	101.129	101.830
M6	30.0	101.735	102.387
M6	32.0	102.390	102.988
M6	34.0	103.097	103.636
	36.0	103.859	104.334
M7	38.0	104.676	105.084
M7	40.0	105.473	105.921
M7	42.0	106.296	106.842
M7	44.0	107.180	107.880
	46.0	108.143	109.023
	48.0	109.190	110.268
	50.0	110.336	111.627
	52.0	111.592	113.117
	54.0	112.975	114.753
	56.0	114.503	116.555
	58.0	116.195	118.542
	60.0	118.076	120.737
	62.0	120.169	123.160
	64.0	122.504	125.836
	66.0	125.110	128.790
	68.0	128.024	132.052
	70.0	131.285	135.654
	72.0	134.938	139.635
	74.0	139.036	144.040
M8	76.0	143.632	148.923
M8	78.0	148.801	154.348
M8	80.0	154.667	160.389
M8	82.0	161.368	167.141
M8	84.0	169.083	174.715
M8	86.0	178.058	183.251
	88.0	188.641	192.923
	90.0	201.308	203.949
	92.0	216.585	216.624

Table A2. - Extraction trajectories for eight ions selected for this study

		.1/25 R(cm)	.3/22 R(cm)	.4/22 R(cm)	.5/22 R(cm)	.5/31.3 R(cm)	.3/41.4 R(cm)	.25/45.5 R(cm)	.1/47.5 R(cm)
	100.0	83.797	83.796	84.171	83.749	86.532	86.429	86.782	85.922
	102.0	84.113	84.141	84.520	84.088	86.743	86.592	86.929	86.079
E1	104.0	84.442	84.502	84.883	84.442	86.957	86.759	87.080	86.240
E1	106.0	84.781	84.872	85.253	84.806	87.170	86.926	87.230	86.404
E1	108.0	85.123	85.245	85.623	85.174	87.380	87.092	87.379	86.566
E1	110.0	85.460	85.612	85.985	85.536	87.582	87.254	87.524	86.725
E1	112.0	85.787	85.965	86.331	85.886	87.775	87.409	87.663	86.878
E1	114.0	86.097	86.298	86.657	86.219	87.955	87.557	87.794	87.024
E1	116.0	86.386	86.609	86.960	86.529	88.123	87.695	87.917	87.161
E1	118.0	86.653	86.895	87.238	86.816	88.277	87.824	88.032	87.289
E1	120.0	86.896	87.153	87.489	87.077	88.416	87.942	88.137	87.406
E1	122.0	87.113	87.384	87.713	87.311	88.540	88.049	88.233	87.513
E1	124.0	87.304	87.586	87.909	87.518	88.650	88.146	88.319	87.609
E1	126.0	87.469	87.760	88.077	87.698	88.744	88.231	88.395	87.694
E1	128.0	87.608	87.904	88.216	87.849	88.823	88.304	88.460	87.767
E1	130.0	87.720	88.019	88.327	87.972	88.887	88.366	88.515	87.829
E1	132.0	87.805	88.105	88.410	88.067	88.936	88.417	88.560	87.878
E1	134.0	87.864	88.162	88.465	88.134	88.969	88.455	88.594	87.917
E1	136.0	87.896	88.189	88.492	88.172	88.987	88.482	88.618	87.943
E1	138.0	87.901	88.187	88.489	88.183	88.989	88.496	88.631	87.957
E1	140.0	87.879	88.156	88.459	88.164	88.976	88.499	88.633	87.959
E1	142.0	87.830	88.094	88.399	88.117	88.948	88.490	88.624	87.949
E1	144.0	87.754	88.002	88.310	88.041	88.904	88.468	88.605	87.926
E1	146.0	87.651	87.879	88.191	87.936	88.844	88.434	88.574	87.892
E1	148.0	87.520	87.725	88.043	87.801	88.769	88.388	88.533	87.845
E1	150.0	87.363	87.541	87.864	87.637	88.678	88.330	88.481	87.786
E1	152.0	87.180	87.328	87.658	87.446	88.573	88.261	88.419	87.716
E1	154.0	86.979	87.094	87.431	87.234	88.458	88.185	88.352	87.639
E1	156.0	86.769	86.848	87.194	87.013	88.341	88.108	88.282	87.559
	158.0	86.556	86.599	86.953	86.788	88.224	88.030	88.214	87.479
	160.0	86.345	86.351	86.715	86.564	88.109	87.955	88.146	87.401
	162.0	86.139	86.108	86.481	86.345	87.999	87.882	88.082	87.327
	164.0	85.942	85.874	86.257	86.135	87.895	87.814	88.023	87.257
	166.0	85.757	85.652	86.045	85.936	87.798	87.752	87.968	87.193
	168.0	85.584	85.444	85.846	85.750	87.710	87.696	87.919	87.135
	170.0	85.425	85.252	85.662	85.579	87.630	87.647	87.876	87.085
	172.0	85.282	85.076	85.494	85.423	87.560	87.604	87.840	87.041
	174.0	85.155	84.918	85.343	85.284	87.500	87.570	87.810	87.006

		.1/25 R(cm)	.3/22 R(cm)	.4/22 R(cm)	.5/22 R(cm)	.5/31.3 R(cm)	.3/41.4 R(cm)	.25/45.5 R(cm)	.1/47.5 R(cm)
	176.0	85.045	84.778	85.211	85.163	87.449	87.542	87.788	86.978
	178.0	84.953	84.658	85.097	85.059	87.410	87.523	87.772	86.958
	180.0	84.879	84.557	85.002	84.974	87.381	87.512	87.764	86.947
	182.0	84.823	84.477	84.926	84.908	87.363	87.509	87.763	86.943
	184.0	84.785	84.417	84.870	84.861	87.356	87.514	87.769	86.949
	186.0	84.766	84.378	84.835	84.834	87.359	87.527	87.783	86.962
	188.0	84.766	84.360	84.819	84.827	87.374	87.549	87.804	86.984
	190.0	84.784	84.363	84.824	84.839	87.400	87.579	87.832	87.015
	192.0	84.821	84.388	84.850	84.871	87.436	87.617	87.868	87.054
	194.0	84.877	84.433	84.895	84.923	87.484	87.663	87.912	87.102
	196.0	84.952	84.500	84.962	84.995	87.542	87.718	87.963	87.158
	198.0	85.045	84.589	85.049	85.087	87.611	87.781	88.021	87.222
	200.0	85.158	84.699	85.157	85.199	87.690	87.852	88.086	87.295
	202.0	85.288	84.830	85.285	85.331	87.781	87.931	88.159	87.376
	204.0	85.437	84.983	85.434	85.482	87.881	88.018	88.240	87.466
	206.0	85.604	85.157	85.603	85.654	87.992	88.113	88.327	87.564
	208.0	85.789	85.353	85.793	85.845	88.113	88.216	88.422	87.670
	210.0	85.992	85.569	86.003	86.055	88.244	88.328	88.524	87.785
	212.0	86.213	85.806	86.232	86.285	88.384	88.447	88.633	87.907
	214.0	86.451	86.064	86.482	86.533	88.535	88.573	88.749	88.038
	216.0	86.706	86.342	86.750	86.800	88.695	88.708	88.872	88.177
	218.0	86.977	86.640	87.037	87.085	88.863	88.849	89.002	88.323
	220.0	87.262	86.955	87.341	87.385	89.040	88.997	89.138	88.476
E2	222.0	87.556	87.282	87.655	87.695	89.220	89.149	89.277	88.634
E2	224.0	87.853	87.613	87.973	88.009	89.400	89.303	89.417	88.793
E2	226.0	88.146	87.942	88.286	88.319	89.578	89.456	89.558	88.952
E2	228.0	88.429	88.260	88.588	88.618	89.750	89.605	89.695	89.108
E2	230.0	88.700	88.563	88.875	88.904	89.916	89.751	89.829	89.259
E2	232.0	88.956	88.849	89.146	89.174	90.074	89.891	89.958	89.405
E2	234.0	89.195	89.117	89.398	89.427	90.224	90.026	90.083	89.544
E2	236.0	89.416	89.365	89.632	89.662	90.364	90.155	90.202	89.678
E2	238.0	89.621	89.594	89.847	89.880	90.496	90.278	90.316	89.805
E2	240.0	89.809	89.804	90.044	90.080	90.620	90.394	90.424	89.925
E2	242.0	89.979	89.995	90.222	90.264	90.734	90.505	90.527	90.039
E2	244.0	90.133	90.167	90.383	90.430	90.840	90.609	90.624	90.145
E2	246.0	90.271	90.321	90.526	90.580	90.937	90.707	90.716	90.245
E2	248.0	90.393	90.458	90.653	90.715	91.026	90.799	90.803	90.339
E2	250.0	90.500	90.577	90.763	90.834	91.107	90.885	90.884	90.425

		.1/25 R(cm)	.3/22 R(cm)	.4/22 R(cm)	.5/22 R(cm)	.5/31.3 R(cm)	.3/41.4 R(cm)	.25/45.5 R(cm)	.1/47.5 R(cm)
E2	252.0	90.592	90.679	90.857	90.938	91.179	90.966	90.960	90.506
E2	254.0	90.669	90.765	90.935	91.028	91.244	91.040	91.031	90.580
E2	256.0	90.732	90.835	90.997	91.103	91.301	91.109	91.096	90.648
E2	258.0	90.781	90.890	91.044	91.164	91.350	91.173	91.157	90.709
E2	260.0	90.816	90.928	91.076	91.212	91.393	91.231	91.213	90.765
E2	262.0	90.838	90.951	91.093	91.246	91.427	91.284	91.265	90.815
	264.0	90.844	90.957	91.093	91.264	91.453	91.330	91.309	90.857
M1	266.0	90.837	90.948	91.079	91.269	91.472	91.370	91.349	90.894
M1	268.0	90.822	90.931	91.058	91.267	91.486	91.407	91.386	90.926
M1	270.0	90.799	90.905	91.029	91.258	91.498	91.441	91.420	90.956
M1	272.0	90.771	90.872	90.995	91.244	91.507	91.473	91.453	90.983
M1	274.0	90.740	90.837	90.958	91.228	91.516	91.505	91.486	91.010
	276.0	90.710	90.801	90.922	91.212	91.526	91.537	91.520	91.037
	278.0	90.679	90.765	90.884	91.194	91.536	91.569	91.553	91.065
M2	280.0	90.650	90.730	90.849	91.177	91.551	91.605	91.590	91.097
M2	282.0	90.626	90.700	90.817	91.164	91.574	91.647	91.634	91.135
M2	284.0	90.607	90.674	90.791	91.155	91.607	91.696	91.684	91.181
	286.0	90.595	90.655	90.770	91.150	91.646	91.751	91.739	91.232
	288.0	90.590	90.642	90.756	91.151	91.690	91.809	91.798	91.287
	290.0	90.592	90.637	90.750	91.159	91.738	91.870	91.859	91.346
	292.0	90.602	90.640	90.750	91.172	91.791	91.934	91.924	91.408
	294.0	90.620	90.650	90.759	91.192	91.848	92.002	91.992	91.475
	296.0	90.647	90.669	90.776	91.219	91.910	92.073	92.064	91.546
	298.0	90.682	90.697	90.801	91.252	91.977	92.148	92.140	91.621
	300.0	90.725	90.732	90.834	91.293	92.049	92.226	92.219	91.700
	302.0	90.777	90.777	90.875	91.340	92.126	92.308	92.301	91.783
	304.0	90.837	90.829	90.925	91.394	92.207	92.394	92.388	91.871
	306.0	90.906	90.891	90.983	91.455	92.293	92.484	92.478	91.963
	308.0	90.983	90.961	91.049	91.523	92.384	92.577	92.571	92.059
	310.0	91.068	91.039	91.123	91.598	92.479	92.674	92.669	92.160
	312.0	91.161	91.126	91.206	91.680	92.580	92.775	92.770	92.265
	314.0	91.262	91.221	91.297	91.769	92.685	92.880	92.875	92.374
	316.0	91.371	91.324	91.396	91.865	92.794	92.988	92.985	92.488
	318.0	91.489	91.437	91.504	91.968	92.909	93.101	93.098	92.607
	320.0	91.614	91.557	91.620	92.078	93.028	93.219	93.216	92.730
	322.0	91.747	91.686	91.744	92.195	93.153	93.340	93.338	92.858
	324.0	91.888	91.824	91.876	92.319	93.282	93.466	93.464	92.991
	326.0	92.038	91.971	92.017	92.451	93.417	93.597	93.595	93.129

		.1/25 R(cm)	.3/22 R(cm)	.4/22 R(cm)	.5/22 R(cm)	.5/31.3 R(cm)	.3/41.4 R(cm)	.25/45.5 R(cm)	.1/47.5 R(cm)
	328.0	92.195	92.126	92.167	92.590	93.557	93.733	93.731	93.272
	330.0	92.361	92.290	92.325	92.737	93.703	93.873	93.872	93.421
	332.0	92.535	92.464	92.492	92.892	93.854	94.020	94.019	93.575
	334.0	92.718	92.647	92.669	93.056	94.012	94.172	94.171	93.736
	336.0	92.909	92.840	92.855	93.228	94.176	94.329	94.329	93.903
	338.0	93.109	93.042	93.051	93.409	94.346	94.493	94.493	94.076
	340.0	93.317	93.253	93.255	93.598	94.522	94.663	94.663	94.255
	342.0	93.533	93.473	93.467	93.794	94.705	94.839	94.839	94.441
	344.0	93.753	93.697	93.684	93.996	94.892	95.020	95.020	94.632
	346.0	93.978	93.927	93.905	94.201	95.084	95.207	95.207	94.829
M3	348.0	94.206	94.160	94.130	94.411	95.282	95.399	95.399	95.031
M3	350.0	94.438	94.398	94.359	94.628	95.486	95.598	95.599	95.241
M3	352.0	94.675	94.640	94.592	94.856	95.700	95.807	95.808	95.460
M3	354.0	94.918	94.888	94.831	95.096	95.925	96.025	96.026	95.689
	356.0	95.166	95.142	95.075	95.345	96.159	96.253	96.253	95.926
M4	358.0	95.421	95.403	95.325	95.601	96.399	96.487	96.488	96.172
M4	0.0	95.687	95.673	95.587	95.869	96.650	96.732	96.733	96.427
M4	2.0	95.969	95.952	95.864	96.152	96.914	96.989	96.989	96.695
M4	4.0	96.267	96.241	96.158	96.452	97.193	97.259	97.259	96.976
	6.0	96.580	96.543	96.467	96.766	97.484	97.542	97.541	97.269
	8.0	96.906	96.857	96.789	97.093	97.787	97.835	97.834	97.574
	10.0	97.246	97.186	97.124	97.434	98.103	98.141	98.139	97.892
	12.0	97.603	97.532	97.474	97.791	98.433	98.461	98.458	98.224
	14.0	97.977	97.894	97.841	98.164	98.778	98.795	98.792	98.570
	16.0	98.370	98.276	98.227	98.556	99.140	99.145	99.141	98.933
M5	18.0	98.785	98.680	98.633	98.969	99.521	99.512	99.507	99.314
M5	20.0	99.226	99.110	99.066	99.404	99.925	99.901	99.895	99.716
M5	22.0	99.701	99.573	99.531	99.864	100.356	100.314	100.306	100.142
M5	24.0	100.210	100.072	100.030	100.351	100.817	100.754	100.744	100.596
	26.0	100.754	100.606	100.563	100.869	101.308	101.221	101.209	101.076
M6	28.0	101.332	101.173	101.129	101.418	101.830	101.716	101.701	101.585
M6	30.0	101.952	101.780	101.735	102.005	102.387	102.244	102.226	102.127
M6	32.0	102.621	102.438	102.390	102.631	102.988	102.809	102.788	102.706
M6	34.0	103.343	103.149	103.097	103.302	103.636	103.418	103.392	103.327
	36.0	104.121	103.915	103.859	104.022	104.334	104.070	104.039	103.993
M7	38.0	104.957	104.737	104.676	104.798	105.084	104.771	104.734	104.706
M7	40.0	105.857	105.623	105.556	105.640	105.897	105.527	105.483	105.473
M7	42.0	106.828	106.580	106.506	106.562	106.783	106.347	106.296	106.305
M7	44.0	107.880	107.616	107.535	107.571	107.751	107.241	107.180	107.207

		.1/25 R(cm)	.3/22 R(cm)	.4/22 R(cm)	.5/22 R(cm)	.5/31.3 R(cm)	.3/41.4 R(cm)	.25/45.5 R(cm)	.1/47.5 R(cm)
	46.0	109.023	108.742	108.654	108.674	108.808	108.213	108.143	108.187
	48.0	110.268	109.969	109.873	109.879	109.963	109.273	109.190	109.253
	50.0	111.627	111.311	111.208	111.199	111.229	110.432	110.336	110.415
	52.0	113.117	112.783	112.672	112.650	112.622	111.704	111.592	111.686
	54.0	114.753	114.403	114.285	114.249	114.159	113.105	112.975	113.083
	56.0	116.555	116.190	116.065	116.018	115.859	114.653	114.503	114.622
	58.0	118.542	118.166	118.036	117.978	117.744	116.369	116.195	116.323
	60.0	120.737	120.353	120.219	120.154	119.838	118.276	118.076	118.208
	62.0	123.160	122.774	122.639	122.568	122.163	120.400	120.169	120.303
	64.0	125.836	125.455	125.320	125.245	124.745	122.769	122.504	122.632
	66.0	128.790	128.419	128.286	128.211	127.609	125.414	125.110	125.229
	68.0	132.052	131.696	131.566	131.491	130.786	128.369	128.024	128.127
	70.0	135.654	135.315	135.189	135.117	134.309	131.676	131.285	131.367
	72.0	139.635	139.314	139.193	139.124	138.218	135.377	134.938	134.991
	74.0	144.040	143.740	143.623	143.558	142.561	139.523	139.036	139.056
M8	76.0	148.923	148.644	148.533	148.472	147.393	144.179	143.645	143.632
M8	78.0	154.348	154.092	153.987	153.931	152.783	149.423	148.848	148.801
M8	80.0	160.389	160.159	160.062	160.012	158.816	155.358	154.748	154.667
M8	82.0	167.141	166.938	166.850	166.807	165.595	162.113	161.480	161.368
M8	84.0	174.715	174.543	174.466	174.431	173.250	169.858	169.222	169.083
M8	86.0	183.251	183.112	183.049	183.024	181.943	178.820	178.216	178.058
	88.0	192.923	192.820	192.773	192.761	191.884	189.315	188.802	188.641
	90.0	203.949	203.885	203.859	203.862	203.333	201.751	201.430	201.308
	92.0	216.610	216.589	216.589	216.611	216.602	216.592	216.599	216.585

References

1) E. Fabrici and A. Salomone, Acceleration Studies for the Milan Superconducting Cyclotron, INFN/TC-83/9, April 1983

2) E. Acerbi et al., The Milan Superconducting Cyclotron Project, Proceedings of the IX International Conference of Cyclotrons and their Applications, Caen (France) 1981, Les Editions de Physique, 1981, pag. 169.

3) G. Bellomo and L. Serafini, Design of the Magnetic Field of the Milan Superconducting Cyclotron, INFN/TC-84/5, March 1984.

4) E. Fabrici and A. Salomone, The Extraction Studies for the Superconducting Cyclotron at the University of Milan, Proceedings of the IX International Conference of Cyclotrons and their Applications, Caen (France),1981 (Les Editions de Physique, 1981), pag. 501.

5) E. Acerbi, F. Alessandria, G. Baccaglioni and L. Rossi, Design of the Main Coils for the Milan Superconducting Cyclotron, Proceedings of the IX International Conference of Cyclotrons and their Applications, Caen (France),1981 (Les Editions de Physique, 1981), pag. 399.

6) E. Fabrici, D. Johnson and F. G. Resmini, The Extraction System for the K-500 Cyclotron at M.S.U., Nuclear Instruments and Methods, 184 (1981) 301.

7) A. Moroni, private communication.

8) C. De Martinis and D. Giove, Proceedings of the X International Conference of Cyclotrons and their Applications, East Lansing (Michigan-USA), IEEE 1984, pag. 575.

9) E. Fabrici, Magnetic Forces on the coils of the Superconducting Cyclotron at the University of Milan, INFN/TC-82/10, July 1982.

10) R. F. Holsinger and C. Iselin, POISCR,The Cern-Poisson program package, Cern computer library T-604, January 1981.

11) M. M. Gordon and D. A. Johnson, Calculation of the Fields in a Superconducting Cyclotron Assuming Uniform Saturation of the Pole Tips, Particles Accelerators, 10 (1980) 217.

12) C. H. Moore, S. K. Howry and H. S. Butler, TRANSPORT, A computer program for designing beam transport system, Stanford University (1964)